



**HAL**  
open science

# On the formulation and implementation of extrinsic cohesive zone models with contact

Nicholas Anton Collins-Craft, Franck Bourrier, Vincent Acary

► **To cite this version:**

Nicholas Anton Collins-Craft, Franck Bourrier, Vincent Acary. On the formulation and implementation of extrinsic cohesive zone models with contact. 2022. hal-03371667v4

**HAL Id: hal-03371667**

**<https://hal.science/hal-03371667v4>**

Preprint submitted on 31 Aug 2022 (v4), last revised 5 Sep 2022 (v5)

**HAL** is a multi-disciplinary open access archive for the deposit and dissemination of scientific research documents, whether they are published or not. The documents may come from teaching and research institutions in France or abroad, or from public or private research centers.

L'archive ouverte pluridisciplinaire **HAL**, est destinée au dépôt et à la diffusion de documents scientifiques de niveau recherche, publiés ou non, émanant des établissements d'enseignement et de recherche français ou étrangers, des laboratoires publics ou privés.

# On the formulation and implementation of extrinsic cohesive zone models with contact

N.A. Collins-Craft<sup>a</sup>, F. Bourrier<sup>a,b</sup>, and V. Acary<sup>a</sup>

<sup>a</sup>Univ. Grenoble Alpes, Inria, CNRS, Grenoble INP, Institute of Engineering, LJK, 38000, Grenoble, France

<sup>b</sup>Univ. Grenoble Alpes, INRAE, ETNA, 38000, Grenoble, France

August 31, 2022

## Contents

<b>1</b>	<b>Introduction</b>	<b>2</b>
<b>2</b>	<b>Formulation of extrinsic cohesive zone models with contact</b>	<b>4</b>
2.1	State variables, powers and principle of virtual power . . . . .	4
2.2	A non-smooth thermo-mechanics potential in the normal direction . . . . .	5
2.3	A linear evolution of the cohesion: triangle law . . . . .	9
<b>3</b>	<b>Non-smooth elasto-dynamics of finite-dimensional systems</b>	<b>11</b>
3.1	Finite-dimensional systems via space-discretisation . . . . .	11
3.2	Non-smooth dynamics and impacts . . . . .	11
<b>4</b>	<b>Numerical time integration</b>	<b>12</b>
4.1	Principles of the time integration scheme . . . . .	13
4.2	Well-posedness of the discrete LCP . . . . .	15
4.3	Discrete energy balance . . . . .	17
<b>5</b>	<b>Numerical validations</b>	<b>18</b>
5.1	Quasi-static scalar case with elastic spring . . . . .	18
5.2	Dynamic cohesive zone model with elasticity . . . . .	20
5.2.1	Dynamic case with single elastic spring . . . . .	20
5.2.2	Dynamic double cantilever beam . . . . .	22
5.2.3	Rhombus hole specimen . . . . .	26
<b>6</b>	<b>Conclusions</b>	<b>30</b>

**Notation** For vectors and tensors, we choose the following notation:

$$\|\mathbf{x}\|^2 = \|x\|^2 = \underbrace{x_i x^i}_{\text{indicial notation}} = \underbrace{\mathbf{x} \cdot \mathbf{x}}_{\text{tensor notation}} = \underbrace{x^\top x}_{\text{vector notation}}. \quad (1)$$

## Abstract

An extrinsic cohesive zone model with a novel unload-reload behaviour is developed in the framework of non-smooth mechanics. The model is extended to include the effects of dynamics with impact, and is discretised in such a way that it can be written as a Linear Complementarity Problem (LCP). This LCP is proved to be well-posed, and to respect the discrete energy balance of the system. Finally, the LCP system is validated numerically, in both statics and dynamics, by simple test cases, and more involved finite element simulations that correspond to standard test geometries in the literature. The results correspond well with those of other authors, while also demonstrating the simulations' ability to resolve with relatively large time steps while respecting the energetic balance.

# 1 Introduction

The modelling of crack propagation touches on a wide variety of areas of interest within mechanics, ranging from a geological scale such as earthquakes and avalanches (Bergfeld et al., 2021; Okubo et al., 2019), engineered materials such as composites (Ashouri Vajari et al., 2013), polymers (Laiarinandrasana et al., 2021) and elastomers (Corre et al., 2021), to the small grains in materials such as sandstone or concrete (Jiang et al., 2021). While linear elastic fracture mechanics (LEFM), pioneered by Griffith (1921), accurately describes significant aspects of crack behaviour, it suffers from the presence of a stress singularity at the crack tip, rendering the model non-physical in the “fracture process zone”, the region surrounding the crack tip. In order to model situations where individual cracks have a large effect on the overall structural behaviour of a system such as fragmentation or dynamic crack branching problems, researchers make use of cohesive zone models (see seminal articles such as Nguyen and Wu (2018), Xu and Needleman (1994), and Zhang et al. (2007)). Cohesive zone models (CZM) regularise the LEFM stress singularity at the crack tip by expressing a relationship between the displacement jump across a developing crack surface and the traction that the surface can support. The total area under the traction-displacement curve represents the classical fracture energy of LEFM (Griffith, 1921). In cohesive zone models the evolution of this interface is described in terms of a cohesion variable  $\beta \in [0, 1]$ , where  $\beta = 1$  indicates a perfectly intact interface, and  $\beta = 0$  a completely broken interface.

Direct experimental observation of the fracture process zone is extremely difficult, due to their typically small size (depending on the material, as small as the order of 10nm (Azab et al., 2020)) and rapid motion. Very few direct observations have been made (C elari e et al., 2003; Guilloateau et al., 1996), although recent work studying the cohesive zones of “frictional cracks” (Berman et al., 2020) offers a promising path towards further direct observations. Due to this difficulty of direct observation, the properties of the cohesive zone are typically inferred via experimental observations at a larger scale, which may require sophisticated image analysis (R ethor e and Estevez, 2013) and the inversion of finite element models (Vargas et al., 2020). It should be noted that the particular values of the inferred parameters such as total fracture energy  $G_c$ , critical traction  $\sigma_c$  and critical length  $\delta_c$  depend on the exact form of the cohesive zone model chosen (Azab et al., 2020). Some inference as to the appropriate form of the model may be drawn by comparing back-analyses of experiments via cohesive zone models with those conducted using other crack analysis techniques such as the coupled criterion, which characterises the initiation of the crack depending on whether it is dominated by the stress across the incipient surface or the stored energy (Doitrand et al., 2019, 2021a).

While the particular form of cohesive zone models is arbitrary and limited only by the modeller’s imagination, in a broad sense they may all be categorised as one of two flavours, intrinsic and extrinsic models. Intrinsic models include an initially elastic response, with an initial strengthening of the cohesive zone as a function of the displacement jump, before weakening due to the decohesion process (Falk et al., 2001). As a consequence, there is an additional length parameter, the hardening length  $\delta_h$ , where the cohesive traction obtains its maximum value (Kubair and Geubelle, 2003). Intrinsic cohesive elements are inserted between the mesh elements before simulation, leading to straightforward computational parallelisation (Nguyen, 2014). However, the elasticity present in the intrinsic model has the effect of modifying the overall elasticity of the structure, with this effect becoming more significant with a greater number of cohesive elements. Thus, intrinsic models introduce an unwanted mesh-dependency to the problem (Falk et al., 2001). The problem of induced artificial compliance can be reduced by increasing the initial hardening slope of the cohesive law. However, in quasi-static analyses, this stiffness increase results in very unstable numerical methods, while in dynamic analyses, it results in severe restrictions on the stable time step size, rendering the method essentially unsuitable (Nguyen, 2014). The presence of interface elasticity also allows for the possibility of interpenetration and physically meaningless negative displacement jumps if the two sides of the interface are pushed together (Acary and Monerie, 2006). Finally, we also note the conceptual impossibility of measuring interface stiffness across a crack face before the crack exists, meaning that any stiffness assigned in an intrinsic model must necessarily be arbitrary and not representative of a true physical property. As such, the stiffness of the intrinsic model is often assumed to be that of the bulk when identifying parameters, and is then taken as a given during the CZM parameter identification procedure (see *e.g.* Vargas et al. (2020)).

On the other hand, extrinsic models are initially rigid and hence immediately start to decohere as the displacement jump increases (Kubair and Geubelle, 2003; Seagraves and Radovitzky, 2010). These models do not effect the elasticity of the bulk, however, typically they are inserted adaptively on-the-fly into finite element meshes (Zhou and Molinari, 2004a), as pre-inserting the elements leads to very large computational overheads due to each node requiring duplicates. Historically the on-the-fly insertion has meant that extrinsic models were difficult to parallelise (Carter et al., 2000), but modern techniques have been developed that have overcome the previous difficulties (Espinha et al., 2013). The absence of artificial stiffness in the extrinsic formulation renders it suitable for use in dynamic analyses due to the absence of artificial compliance effects (Camacho and Ortiz, 1996; Murphy and Ivankovic, 2005; Seagraves and Radovitzky, 2010), but care must be taken to ensure that the system exhibits time-continuous behaviour (Papoulia et al., 2003; Sam et al., 2005). A modified Lagrangian formulation can ensure this time-continuity (Cazes et al., 2013). While extrinsic models do not have the pathological mesh-dependency of intrinsic models, the large number of elements required to fully resolve the cohesive zone for arbitrary crack paths has been impractical, meaning that simulations are typically not fully converged. This issue can be at least partially addressed by modelling cohesive zone strength via a Weibull distribution (Zhou and Molinari, 2004a,b). The use of more sophisticated finite element techniques such as those based on the partition of unity (Bybordiani and Dias-da-Costa, 2021), Hybrid Equilibrium Elements (Parrinello,

2020; Parrinello and Borino, 2020), or Discontinuous Galerkin (Nguyen, 2014; Versino et al., 2015) constitutes a promising path towards truly mesh-independent results.

However, extrinsic cohesive zone models implemented on a highly-refined mesh can still suffer from issues of ill-posedness (Fouk, 2010). In quasi-statics, solution jumps can appear due to the elasticity of the system storing more energy than can be released by the cohesive zone (Acary and Monerie, 2006). This issue has been addressed using either sophisticated enriched finite element schemes (Samimi et al., 2011) or viscous regularisation (Chaboche et al., 2001), in order to ensure that the problem remains well-posed.

We must also pay close attention to the unload-reload behaviour of models, particularly in cases of non-monotonic loading e.g. repeated impacts or complex stress wave patterns, where cohesive elements may incur only partial decohesion before being subjected to unloading and reloading. By considering the mathematical structure detailed in Kubair and Geubelle (2003), where by shifting the values of model parameters both intrinsic and extrinsic models may be obtained from the same formula, we may define the notion of a “shifted intrinsic model”, where the extrinsic model retains an underlying intrinsic mathematical structure. Typically extrinsic models indicate that after the cohesion has decreased, the unload-reload behaviour is elastic until decohesion recommences (Bybordiani and Dias-da-Costa, 2021; Camacho and Ortiz, 1996; Parrinello, 2020; Parrinello and Borino, 2020; Sam et al., 2005). Models exhibiting this behaviour constitute shifted intrinsic models where the *effective* critical traction  $\sigma_{c,e}$  and hardening length  $\delta_h$  are shifted away from their initial values ( $\sigma_c$  and 0 respectively) as the cohesion  $\beta$  evolves. For this family of models, the unload-reload elasticity can be approximated by  $E \approx \tan\left(\beta\frac{\pi}{2}\right)$ . It is clear that for very small amounts of decohesion with  $\beta \approx 1$ , the elasticity of the interface is arbitrarily large and the problems of artificial compliance inherent to intrinsic models may also arise in extrinsic models if they have the shifted intrinsic model structure.

Thus, we may conclude that an extrinsic model is the most appropriate to model crack behaviour, but special care must be taken to avoid unphysical behaviour at the interface in both the initial loading phase, and for cases of unloading and reloading. An extrinsic cohesive model may be naively viewed as an interface model with an infinite initial stiffness. The correct mathematical setting to impose such a constraint is convex and variational analysis, exploiting the techniques of mathematical programming. To this end, we turn to the field of contact mechanics, in particular the seminal work of Moreau (Moreau, 1970, 1974, 1986), who developed the mathematical framework of non-smooth mechanics. By appropriately specifying the potential of energy and the pseudo-potential of dissipation within the framework of convex analysis, rigorous thermodynamic formulations for a range of materials may be developed (Halphen and Nguyen, 1975; Houlsby, 2019; Marigo, 1981) including unilateral constraints on the variables and their time derivatives. In particular, this family of models has been extended to cohesive zone modelling in a series of seminal works by Frémond (Frémond, 1988, 2002, 2012a,b), which provides a natural framework in which we present our models. The pioneering work of Frémond has already been extended in various directions for intrinsic cohesive zone models (Acary and Monerie, 2006; Chaboche et al., 2001; Monerie and Acary, 2001; Nkoubou Kaptchouang et al., 2021; Perales et al., 2010; Raous et al., 1999) but has been barely used for extrinsic models other than those of Jean et al. (2001) and Talon and Curnier (2003). We note that in the latter formulation, the model does not suffer from the issues raised by the shifted intrinsic model structure, unlike those models developed following Camacho and Ortiz (1996) (amongst others).

An alternative approach where extrinsic cohesive models appear naturally is the variational approach to fracture (Bourdin et al., 2008; Charlotte et al., 2006; Del Piero, 1999). The equilibrium of a fractured system is formulated as an energy-minimisation principle. The constitutive law for cohesion is defined by the surface energy that is created when the fracture progresses, as a concave function of the displacement jump. This surface energy converges asymptotically to the fracture toughness when the interface is completely broken. The derivative of the surface energy at the origin with respect to the displacement jump defines the critical strength of the interface. The constitutive law is completed with a law that accounts for the irreversibility of the process, and is implemented in an incremental form of the energy minimisation. As in the classical cohesive theory of fracture, there is no initial stiffness. The optimality conditions (or stationarity conditions if we prefer) yield the definition of an extrinsic cohesive zone model. The theory, in quasi-statics, demonstrates that some energy jumps are possible in specific cases that match those observed in the classical formulation of cohesive zone models.

Following this original idea, numerical methods have been designed to simulate fracture problems by combining energy minimisation and extrinsic cohesive zone models. In one of the most advanced works (Lorentz, 2008), the unilateral contact condition is added by means of an augmented Lagrangian that helps to retrieve convexity at the price of needing to correctly determine the exact penalty parameter. To model this irreversibility process, the model developed in Talon and Curnier (2003) is used. A finite element discretisation based on a mortar-like approach is solved by a non-smooth Newton method. A time-stepping is then implemented using a solver based on an alternate minimisation fixed point. In Doyen et al. (2010), a mathematical analysis of a similar model with mixed elements is proposed. Although the discrete minimisation is non-convex, the convergence study of numerical methods such as Uzawa and non-smooth Newton methods is performed. In Papoulia (2017) and Vavasis et al. (2020), a very similar approach is developed, taking into account the inertia effects in discrete time and using modern optimisation methods. Nevertheless, the irreversibility process is modelled in the same fashion as in Camacho and Ortiz (1996) and hence leads to the same issues. The minimisation principle is based on the non-convex energy which includes the constraints (unilateral contact, irreversibility) using non-smooth and non-differentiable functions.

To situate our work with respect to the variational approach to fracture, we note that our differences mainly lie in the methodology, which leads to rather different properties for the numerical scheme. In our work, we start from a consistent mechanical model and use the laws of thermodynamics in a non-smooth setting. This leads to variational inequalities or complementarity problems that can accommodate a wide variety of models, but these problem formulations are not necessarily equivalent to the optimality conditions of an optimisation problem. In other words, the variational inequality is not necessarily the optimality condition of a minimisation problem. In some structured cases, variational inequalities and complementarity problems can be recast into (possibly convex) optimisation problems, but their mechanical interpretation may be difficult. To place our framework in a minimisation setting that can play the role of a mechanical principle, further investigations are needed, which are beyond the scope of the paper.

To complete this brief review of the literature, the closest work to our approach is developed in Doyen et al. (2013), where an extrinsic cohesive zone model in dynamics with unilateral constraints is proposed. Two models of irreversibility are used. One is similar to the Camacho and Ortiz (1996) model and the other to the Talon and Curnier (2003) model. Using an explicit evaluation of some interface variables, they are able to show that the discrete problem is well-posed at each time step given some mild assumptions on the time step and the mesh size. Discrete energy balances are also provided, but they are not directly related to the fracture energy. The method has been extended in Crump et al. (2017) in the context of the extended finite element method to enable the developments of cracks not only at the boundary of the mesh elements, and in Marazzato (2020) in the context of a variational discrete element method. However, the proposed scheme does not take into account the possible appearance of percussions due to velocity jumps. This latter discrete property is important when dealing with finite masses (e.g rigid bodies, the discrete element method, slender structures or space-discretised structures). The aim of our paper is to bridge this gap.

**Novelty of the contribution and outline of the article:** The novelty of our work is that we present the formulation of an extrinsic cohesive zone model that provides us with:

1. a formulation based on non-smooth thermo-mechanics principles that take into account the effects of inertia and the inequality constraints on state variables and their time derivatives (unilateral contact, irreversibility) with a simple loading/unloading behaviour related to the irreversibility of the process which does not have the issues of the shifted intrinsic model structure or the problem of infinite stiffness (§2), and
2. a formulation of the non-smooth dynamics in a finite-dimensional setting in terms of differential measures that takes into account the effect of inertia and the possibility of discontinuities in the velocity and the associated percussion together with an impact law (§3),

and a numerical procedure in §4 that features the following properties:

1. an implicit time-stepping scheme consistent with the non-smooth dynamics based on the Moreau–Jean scheme, that respects the energy balance in discrete time, and which provides us with a stable scheme with quite large time steps,
2. a complementarity problem formulation for the space and time discretised problem with a proof of well-posedness (existence and uniqueness of solutions) that solves all of the constraints in an implicit manner; in that way, the extrinsic cohesive model is satisfied at each time step while avoiding the solution jumps that occur in quasi-statics when the cohesive model is not regularised by viscous or second gradient techniques, and
3. a formulation as a monolithic complementarity problem allowing us to exploit the efficient algorithms that have been developed for this class of problems in the mathematical programming literature.

Finally, we demonstrate the interest of the approach in §5 by applying the model to some pertinent example systems and compare the results with those obtained by other workers.

## 2 Formulation of extrinsic cohesive zone models with contact

In this section, we define the state variables of the system, obtain the equilibrium and boundary conditions via the principle of virtual power, specify the constitutive model, and demonstrate its behaviour with an analytic example.

### 2.1 State variables, powers and principle of virtual power

We start by defining our system. Let us consider a body defined by  $\Omega \in \mathbb{R}^d$ ,  $d \in \llbracket 1, 3 \rrbracket$ . The vector  $\boldsymbol{x}$  defines the current position and  $\boldsymbol{X}$  the initial position,  $\boldsymbol{u}(\boldsymbol{x})$  the displacement and  $\boldsymbol{v}(\boldsymbol{x}) = \dot{\boldsymbol{u}}(\boldsymbol{x})$  the velocity. The definition of the displacement jump at the interface is not trivial in practice. In this work, we consider that, initially, the material is undamaged. At a point  $\boldsymbol{x} \in \Omega$ ,  $\boldsymbol{x} \in \mathbb{R}^d$ , the displacement  $\boldsymbol{u}(\boldsymbol{x})$  and the velocity  $\boldsymbol{v}(\boldsymbol{x})$  are continuously differentiable functions of  $\boldsymbol{x}$ . If a crack occurs and an interface is created, two material points  $\boldsymbol{x}_l$  and  $\boldsymbol{x}_r$  are defined by splitting the bodies assuming that they correspond to the material point  $\boldsymbol{X}$  initially. We choose to denote  $\boldsymbol{x}_l$  by  $\boldsymbol{x}$ . The displacement jump is defined by the difference in the position

of the material point that was at  $\mathbf{X}$  initially, with respect to  $\mathbf{x}$  and  $\mathbf{x}_r$ , that is  $[[\mathbf{u}(\mathbf{x}, \mathbf{x}_r)]] = \mathbf{u}(\mathbf{x}_r) - \mathbf{u}(\mathbf{x})$ . We also assume that we are able to define an orthonormal local frame at any point  $\mathbf{x}$  of the interface defined by  $(\mathbf{x}, \mathbf{n}, \mathbf{t})$  where  $\mathbf{n} \in \mathbb{R}^d$  is the normal unit vector from  $\mathbf{x}$  towards  $\mathbf{x}_r$  and the vector  $\mathbf{t} = [\mathbf{t}_1, \mathbf{t}_2] \in \mathbb{R}^{d \times (d-1)}$  completes the frame. In this work, we consider only the normal displacement (jump), defined by  $u_N(\mathbf{x}, \mathbf{x}_r) = [[\mathbf{u}(\mathbf{x}, \mathbf{x}_r)]] \cdot \mathbf{n} \in \mathbb{R}$ . The relative velocity (jump in space) is defined as  $v_N = \dot{u}_N$ . Before the creation of the interface, we assume that  $u_N$  and  $v_N$  vanish whatever the arbitrary definition of the local frame since  $\mathbf{u}$  and  $\mathbf{v}$  are continuous.

To describe the state of the cohesion we introduce the cohesion variable  $\beta(\mathbf{x}) \in [0, 1]$ , using the notation introduced by Frémond for describing the intensity of cohesion, or the proportion of active bonds. For a point  $\mathbf{x}$  on the interface, the power of the cohesion for a surface  $\Gamma$  is defined by

$$\mathcal{P}_{\text{coh}} = \int_{\Gamma} \dot{\beta} A \, dx, \quad (2)$$

introducing  $A$  which is the dual force (driving force) associated to  $\beta$ . In the same way, the power of contact is given by

$$\mathcal{P}_{\text{con}} = \int_{\Gamma} v_N r_N \, dx, \quad (3)$$

introducing  $r_N$  as the normal reaction force related to the stress  $\boldsymbol{\sigma}(\mathbf{x})$  at the interface by  $r_N = -\boldsymbol{\sigma} \cdot \mathbf{n} \cdot \mathbf{n}$ .

For the material in  $\Omega$ , the power of the external, internal and inertial forces are respectively given by

$$\mathcal{P}_{\text{ext}} = \int_{\Omega} \mathbf{v} \cdot \mathbf{f} \, dx - \int_{\Gamma_{\mathcal{N}}} \mathbf{v} \cdot \boldsymbol{\tau} \, dx - \int_{\Gamma} \dot{\beta} \Theta \, dx, \quad (4)$$

$$\mathcal{P}_{\text{int}} = - \int_{\Omega} \boldsymbol{\sigma} : \dot{\boldsymbol{\varepsilon}} \, dx + \int_{\Gamma} v_N r_N \, dx + \int_{\Gamma} \dot{\beta} A \, dx, \quad (5)$$

$$\mathcal{P}_{\text{acc}} = \int_{\Omega} \rho \mathbf{v} \cdot \dot{\mathbf{v}} \, dx, \quad (6)$$

where  $\mathbf{f}$  is the body force in  $\Omega$ ,  $\boldsymbol{\tau}$  is the surface traction on  $\Gamma_{\mathcal{N}}$  (*i.e.* where the Neumann boundary condition is applied on the surface),  $\Theta$  is an external force that does work on the cohesion (such as may arise from thermal or chemical effects) that is taken as identically zero in this work,  $\boldsymbol{\varepsilon}$  is the strain in  $\Omega$ ,  $\rho$  is the density and  $\dot{\mathbf{v}}$  is the acceleration.

The principle of virtual power states that for any virtual velocities  $\bar{\mathbf{v}}$ ,  $\dot{\bar{\boldsymbol{\varepsilon}}}$  and  $\dot{\bar{\beta}}$ , we have

$$\begin{aligned} \bar{\mathcal{P}}_{\text{acc}} &= \bar{\mathcal{P}}_{\text{ext}} + \bar{\mathcal{P}}_{\text{int}}, \\ \int_{\Omega} \rho \bar{\mathbf{v}} \cdot \dot{\mathbf{v}} \, dx &= \int_{\Omega} \bar{\mathbf{v}} \cdot \mathbf{f} \, dx - \int_{\Gamma_{\mathcal{N}}} \bar{\mathbf{v}} \cdot \boldsymbol{\tau} \, dx - \int_{\Gamma} \dot{\bar{\beta}} \Theta \, dx - \int_{\Omega} \boldsymbol{\sigma} : \dot{\bar{\boldsymbol{\varepsilon}}} \, dx + \int_{\Gamma} \bar{v}_N r_N \, dx + \int_{\Gamma} \dot{\bar{\beta}} A \, dx. \end{aligned} \quad (7)$$

For a rigorous mathematical setting of this principle, we refer to Frémond (1988). Using sufficient smoothness assumptions on the fields, this leads by localisation to the set of equations describing the equilibrium and boundary conditions of the system:

$$\left\{ \begin{array}{ll} \nabla \cdot \boldsymbol{\sigma} + \mathbf{f} = \rho \dot{\mathbf{v}} & \text{in } \Omega, \\ A = \Theta = 0 & \text{on } \Gamma, \\ \boldsymbol{\tau} = \boldsymbol{\sigma} \cdot \mathbf{n} & \text{on } \Gamma_{\mathcal{N}}, \\ r_N = -\boldsymbol{\sigma} \cdot \mathbf{n} \cdot \mathbf{n} & \text{on } \Gamma. \end{array} \right. \quad (8)$$

## 2.2 A non-smooth thermo-mechanics potential in the normal direction

Now, we specify our constitutive model via the appropriate specification of an energy potential, and a dissipation pseudo-potential. We will also show that the system can be written in terms of complementarity relations, and use this to derive an expression for the energy balance.

**Free energy and reversible state laws.** The free energy  $\Psi$  of the system is the sum of the free energy in the bulk with that of the surface, that is

$$\Psi = \int_{\Omega} \Psi_e(\boldsymbol{\varepsilon}) \, dx + \int_{\Gamma} \Psi_s(u_N, \beta) \, dx, \quad (9)$$

where  $\Psi_e$  and  $\Psi_s$  are the volume and surface free energies. In this work, we assume all strain is elastic. Firstly, the stresses may be obtained by assuming a classical linear elastic potential for the bulk:

$$\Psi_e(\boldsymbol{\varepsilon}) = \frac{1}{2} \boldsymbol{\varepsilon} : \mathbf{E} : \boldsymbol{\varepsilon}, \quad (10)$$

$$\boldsymbol{\sigma}(\boldsymbol{\varepsilon}) = \frac{\partial \Psi_e(\boldsymbol{\varepsilon})}{\partial \boldsymbol{\varepsilon}} = \mathbf{E} : \boldsymbol{\varepsilon}, \quad (11)$$

where  $\mathbf{E}$  is a fourth order stiffness tensor. The stress-like variables are similarly derived from the surface potential by

$$\begin{cases} -r_N^r \in \partial_{u_N} \Psi_s(u_N, \beta), \\ -A^r \in \partial_\beta \Psi_s(u_N, \beta), \end{cases} \quad (12)$$

where  $r_N^r$  stands for the reversible part of the normal reaction force, and  $\partial_{u_N}$  and  $\partial_\beta$  indicate the subdifferentials with respect to  $u_N$  and  $\beta$  of a convex (or concave) but non-smooth potential (Frémond, 2002). The first assumption in our model is that the displacement is constrained to be positive,  $u_N \geq 0$ , which is enforced as a unilateral constraint, and the cohesion variable constraints are  $0 \leq \beta \leq 1$ . This yields the possible form of the surface free energy

$$\Psi_s(u_N, \beta) = \psi(u_N, \beta) + \mathcal{I}_{\mathbb{R}_+}(u_N) + \mathcal{I}_{[0,1]}(\beta), \quad (13)$$

where  $\mathcal{I}_C$  is the indicator function of a convex set  $C$ . To obtain an extrinsic CZM, the tangent stiffness of the model when  $u_N \geq 0$  must vanish. In other words, the derivative of  $\psi(u_N, \beta)$  with respect to  $u_N$  must be constant, i.e.  $\frac{\partial^2 \psi}{\partial u_N^2} = 0$ . The simplest choice for the free energy is:

$$\Psi_s(u_N, \beta) = \beta \sigma_c u_N + w f(\beta) + \mathcal{I}_{\mathbb{R}_+}(u_N) + \mathcal{I}_{[0,1]}(\beta), \quad (14)$$

where

- $\sigma_c > 0$  is the critical traction,
- $w > 0$  is the surface free energy which is released by decohesion, and
- $f(\beta)$  is a function that enables us to parametrise the evolution of  $\beta$  in the decohesion process.

The state laws are deduced by applying (12) to (14):

$$\begin{cases} -(r_N^r + \beta \sigma_c) \in \partial \mathcal{I}_{\mathbb{R}_+}(u_N), \\ -(A^r + \sigma_c u_N + w f'(\beta)) \in \partial \mathcal{I}_{[0,1]}(\beta). \end{cases} \quad (15)$$

The first law in (15) is a shifted Signorini condition by the value of the cohesive force defined by  $r_N^c(\beta) = \beta \sigma_c$ . This can be written in terms of a complementarity relation:

$$0 \leq r_N^r + r_N^c(\beta) \perp u_N \geq 0. \quad (16)$$

The surface free energy  $\Psi_s$  is not a convex function of its arguments  $(u_N, \beta)$  since the determinant of its Hessian matrix is equal to  $-\sigma_c^2$ . Nevertheless  $\Psi_s$  is convex with respect to  $u_N$  since it is linear. By choosing  $f''(\beta) \geq 0$ , the convexity with respect to  $\beta$  is ensured. The smooth part of the free energy in (14) is composed of two terms. The first term  $\beta \sigma_c u_N$  is homogeneous to a potential energy given by the cohesive force  $\beta \sigma_c$  in the displacement field  $u_N$ . The second term  $w f(\beta)$  is the surface free energy released by decohesion for a given  $\beta$ . Some further modelling assumptions may also be specified on the function  $f$ . For an intact interface ( $\beta = 1$ ), we may assume that  $f(1) = 0$  such that the released free energy vanishes. For a broken interface ( $\beta = 0$ ), we may assume that the cohesive free energy  $w$  has completely been released then  $f(0) = 1$ . Furthermore, we may also assume a monotone release for the cohesion free energy with  $\beta$ , that  $f'(\beta) \leq 0$ . This choice is consistent with the convexity of  $f$  if the minimum is attained for  $\beta = 1$ . In the following, these assumptions will be satisfied by the triangle law we propose.

**Dissipation pseudo-potential and irreversible processes.** To define the irreversibility of the process of decohesion in a way consistent with the second law of thermodynamics, the dissipation function, defined for an isothermal process as

$$\mathcal{D} = -\mathcal{P}_{\text{int}} - \int_{\Omega} \dot{\Psi}_e(\varepsilon) dx - \int_{\Gamma} \dot{\Psi}_s(u_N, \beta), \quad (17)$$

must be non-negative. The computation of the time derivative of the non-smooth and non-convex potential requires some care. The functions  $u_N(t)$  and  $\beta(t)$  are assumed to be absolutely continuous, and hence they have a derivative almost everywhere but not necessarily at any given point. Since absolutely continuous functions are of bounded variations, their left and right derivatives exist. Assuming  $\Psi_s$  is convex in  $u_N$  and in  $\beta$  separately, and  $\dot{\Psi}_s(u_N, \beta)$  is also an absolutely continuous function for  $u_N \geq 0, \beta \in [0, 1]$ , a result in Frémond (2002, Appendix A.1.9) provides us with the following inequality:

$$\dot{\Psi}_s(u_N, \beta) \leq -v_N r_N^r - \dot{\beta} A^r, \quad (18)$$

for any  $r_N^r$  and  $\dot{\beta}$  that satisfies the inclusions (15).<sup>1</sup> Substituting this inequality in the definition of the dissipation yields,

$$\mathcal{D} \geq \int_{\Omega} \boldsymbol{\sigma} : \dot{\boldsymbol{\varepsilon}} dx - \int_{\Gamma} (v_N r_N^r + \dot{\beta} A) dx - \int_{\Omega} \frac{\partial \Psi_e(\varepsilon)}{\partial \varepsilon} \dot{\boldsymbol{\varepsilon}} dx + \int_{\Gamma} (v_N r_N^r + \dot{\beta} A^r) dx. \quad (19)$$

<sup>1</sup>To avoid complicated notation, we do not mention left or right derivatives.

In (19), the terms integrated over  $\Omega$  cancel out. We then obtain

$$\mathcal{D} \geq \int_{\Gamma} \left( -v_N r_N - \dot{\beta} A + v_N r_N^r + \dot{\beta} A^r \right) dx. \quad (20)$$

Since we want to ensure that  $\mathcal{D} \geq 0$ , we will assume that

$$-v_N r_N - \dot{\beta} A + v_N r_N^r + \dot{\beta} A^r \geq 0, \text{ or equivalently, } -v_N r_N^{\text{ir}} - \dot{\beta} A^{\text{ir}} \geq 0, \quad (21)$$

using the standard decomposition  $r_N = r_N^r + r_N^{\text{ir}}$  and  $A = A^r + A^{\text{ir}}$  for the irreversible parts of the stress-like variables. A standard way to ensure this inequality is to postulate the existence of a proper closed convex pseudo-potential<sup>2</sup> of dissipation  $\Phi(v_N, \dot{\beta})$  such that the dissipation process is governed by

$$\begin{cases} -r_N^{\text{ir}} \in \partial_{v_N} \Phi(v_N, \dot{\beta}), \\ -A^{\text{ir}} \in \partial_{\dot{\beta}} \Phi(v_N, \dot{\beta}). \end{cases} \quad (22)$$

Let us assume that the dissipation process is only governed by the rate of  $\beta$ . We can choose for the pseudo-potential of dissipation

$$\Phi(v_N, \dot{\beta}) = \mathcal{I}_{\mathbb{R}_-}(\dot{\beta}). \quad (23)$$

This model of dissipation only imposes that the evolution of  $\beta$  must decrease with time, i.e.  $\dot{\beta} \leq 0$ . The dissipative laws are thus

$$\begin{cases} -r_N^{\text{ir}} = 0, \\ -A^{\text{ir}} \in \partial \mathcal{I}_{\mathbb{R}_-}(\dot{\beta}). \end{cases} \quad (24)$$

Equivalently, the last line of (24) can be written as

$$\dot{\beta} \in \partial \mathcal{I}_{\mathbb{R}_+}(-A^{\text{ir}}). \quad (25)$$

In this form, we can easily interpret that  $A^{\text{ir}}$  is the force that drives the evolution of  $\beta$ . Given that in (8),  $A = 0$ , we must have  $A^r = -A^{\text{ir}}$ , and thus

$$\dot{\beta} \in \partial \mathcal{I}_{\mathbb{R}_+}(A^r). \quad (26)$$

**Remark 1.** *The choice of the pseudo-potential (23) results in a model that is rate independent. A rate dependency can be easily added here by considering a model that is non-linear in the rates of the dissipative variables, such as*

$$\Phi(v_N, \dot{\beta}) = \frac{c}{p+1} (-\dot{\beta})^{p+1} + \mathcal{I}_{\mathbb{R}_-}(\dot{\beta}), \quad (27)$$

where the coefficient  $c$  is a viscosity and  $p$  a given parameter for the non-linear viscosity (Acary and Monerie, 2006).

**Complete extrinsic cohesive zone model.** Noting that  $r_N = r_N^r$ , the complete model of the interface is given by

$$\begin{cases} \dot{\beta} \in \partial \mathcal{I}_{\mathbb{R}_+}(A^r), \\ -(r_N + \beta \sigma_c) \in \partial \mathcal{I}_{\mathbb{R}_+}(u_N), \\ -(w f'(\beta) + \sigma_c u_N + A^r) \in \partial \mathcal{I}_{[0,1]}(\beta). \end{cases} \quad (28)$$

We highlight that as  $r_N^{\text{ir}} = 0$  and (26) implies one of  $\dot{\beta}$  or  $A^r$  is always zero, (21) is also zero. While the process of decohesion and surface creation is irreversible, it is also non-dissipative in the sense that  $-v_N r_N^{\text{ir}} - \dot{\beta} A^{\text{ir}} = 0$ .

**Variational inequality and complementarity problem.** The system can be formulated as an evolution variational inequality by

$$-F(\dot{\beta}, \beta, u_N, r_N, A^r) \in N_{\mathbb{R}_+ \times \mathbb{R}_+ \times [0,1]} \left( \begin{bmatrix} A^r \\ u_N \\ \beta \end{bmatrix} \right), \text{ with } F(\dot{\beta}, \beta, u_N, r_N, A^r) = \begin{bmatrix} -\dot{\beta} \\ r_N + \beta \sigma_c \\ w f'(\beta) + \sigma_c u_N + A^r \end{bmatrix}. \quad (29)$$

<sup>2</sup>a closed convex function is a convex function that is lower-semi continuous, or equivalently its epigraph is a closed convex set

Introducing slack variables  $\mu$ ,  $\lambda$ , and  $\nu$ , this system can also be formalised using normal cones to convex sets as

$$\begin{cases} \dot{\beta} = -\lambda, & wf'(\beta) + \sigma_c u_N + A^r = \mu, & r_N + \beta \sigma_c = \nu, \\ -\nu \in N_{\mathbb{R}_+}(u_N), & -\mu \in N_{[0,1]}(\beta), & -\lambda \in N_{\mathbb{R}_+}(A^r). \end{cases} \quad (30)$$

Using the definition of a normal cone to a convex set defined by simple bounds, this model can be written with complementarity conditions as a Mixed Complementarity System (MCS):

$$\begin{cases} \dot{\beta} = -\lambda, & wf'(\beta) + \sigma_c u_N + A^r = \mu, & r_N + \beta \sigma_c = \nu, & \mu = \mu_+ - \mu_-, \\ 0 \leq \nu \perp u_N \geq 0, & 0 \leq \mu_+ \perp \beta \geq 0, & 0 \leq \mu_- \perp 1 - \beta \geq 0, & 0 \leq \lambda \perp A^r \geq 0. \end{cases} \quad (31)$$

**Energy Balance** With the chosen constitutive laws, the power of internal forces can be written as

$$\begin{aligned} \mathcal{P}_{\text{int}} &= - \int_{\Omega} \varepsilon : \mathbf{E} : \dot{\varepsilon} \, dx + \int_{\Gamma} r_N v_N \, dx + \int_{\Gamma} A \dot{\beta} \, dx, \\ &= - \frac{d}{dt} \left( \int_{\Omega} \varepsilon : \mathbf{E} : \varepsilon \, dx \right) + \int_{\Gamma} (r_N v_N + A \dot{\beta}) \, dx, \\ &= -\dot{\mathcal{U}} + \mathcal{P}_{s,\text{int}}, \end{aligned} \quad (32)$$

where  $\mathcal{U}$  is the potential elastic strain energy, and  $\mathcal{P}_{s,\text{int}}$  the power of surface internal forces defined by  $\mathcal{P}_{s,\text{int}} = \int_{\Gamma} (r_N v_N + A \dot{\beta}) \, dx$ .

Using the constitutive laws (30), we have

$$\begin{aligned} 0 &= v_N r_N^{\text{ir}} + \dot{\beta} A^{\text{ir}}, \\ &= v_N r_N + \dot{\beta} A - v_N (\nu - \beta \sigma_c) - \dot{\beta} (\mu - \sigma_c u_N - wf'(\beta)). \end{aligned} \quad (33)$$

Since  $-\nu \in N_{\mathbb{R}_+}(u_N)$  and  $-\mu \in N_{[0,1]}(\beta)$ , we have  $\nu v_N = 0$  and  $\mu \dot{\beta} = 0$  almost everywhere, the expression (33) can be simplified to

$$\begin{aligned} 0 &= v_N r_N + \dot{\beta} A + v_N \beta \sigma_c + \dot{\beta} (\sigma_c u_N - wf'(\beta)), \\ &= v_N r_N + \dot{\beta} A + v_N \frac{\partial \psi}{\partial u_N} + \dot{\beta} \frac{\partial \psi}{\partial \beta}, \\ &= v_N r_N + \dot{\beta} A + \dot{\psi}. \end{aligned} \quad (34)$$

We deduce that the power of surface internal forces is equal, almost everywhere, to the change of the smooth part of the free energy

$$\mathcal{P}_{s,\text{int}} = - \int_{\Gamma} \dot{\psi} \, dx = \int_{\Gamma} \beta \sigma_c v_N \, dx. \quad (35)$$

Using the principle of virtual power for the actual velocities of the system, the energy balance,  $\dot{\mathcal{K}} = \mathcal{P}_{\text{ext}} + \mathcal{P}_{\text{int}}$  is almost everywhere

$$\dot{\mathcal{K}} + \dot{\mathcal{U}} + \int_{\Gamma} \dot{\psi} \, dx = \mathcal{P}_{\text{ext}}, \quad (36)$$

where  $\mathcal{K}$  is the kinetic energy. The first law of thermodynamics in an isothermal setting results in the energy balance  $\dot{\mathcal{K}} + \dot{\mathcal{E}} = \mathcal{P}_{\text{ext}}$ , where  $\mathcal{E}$  is the internal energy. A simple identification shows that

$$\dot{\mathcal{E}} = -\mathcal{P}_{\text{int}} = \int_{\Gamma} \dot{\psi} \, dx + \dot{\mathcal{U}}. \quad (37)$$

Since  $\Psi_s = \psi$  for all admissible  $u_N, \beta$ , we obtain that the fracture energy is given by

$$\mathcal{G} = \int \int_{\Gamma} \beta \sigma_c v_N \, dx \, dt = - \int \int_{\Gamma} \dot{\psi} \, dx \, dt = - \int \int_{\Gamma} \dot{\Psi}_s \, dx \, dt. \quad (38)$$

The following incremental energy balance can be then written as

$$\Delta \mathcal{K} + \Delta \mathcal{U} + \Delta \mathcal{G} = \int_{t_1}^{t_2} \mathcal{P}_{\text{ext}} \, dt, \text{ and } \Delta \mathcal{E} = \Delta \mathcal{U} + \Delta \mathcal{G}. \quad (39)$$

**Remark 2.** For an evolution from an intact interface with  $u_N = 0, \beta = 1$  to a broken interface  $\beta = 0$  on  $\Gamma$ , we get from (38) that

$$\Delta \mathcal{G} = \int_{\Gamma} w \, dx.$$

### 2.3 A linear evolution of the cohesion: triangle law

We now specify the exact form of the surface potential. We require that when the surface doesn't exist, *i.e.*  $u_N = 0$  and  $\beta = 1$ ,  $\Psi_s = 0$ , and that when the surface is fully decohered, *i.e.*  $\beta = 0$ ,  $\Psi_s = w$ . We assume that this decohesion is complete at a critical length  $\delta_c > 0$ . Choosing

$$\begin{cases} w = \frac{\sigma_c \delta_c}{2}, \\ f(\beta) = (\beta - 1)^2, \end{cases} \quad (40)$$

fulfils the required conditions for the energy while ensuring that the potential remains convex in  $\beta$ . While  $\beta \in [0, 1]$  and  $\dot{\beta} < 0$ , the second term in (31) gives  $\beta = 1 - \frac{u_N}{\delta_c}$ . Substituting this displacement-cohesion law into the free energy, we get:

$$\Psi_s(u_N) = \sigma_c u_N - \frac{\sigma_c u_N^2}{2\delta_c} + \mathcal{I}_{\mathbb{R}_+}(u_N) + \mathcal{I}_{[0,1]}\left(1 - \frac{u_N}{\delta_c}\right). \quad (41)$$

The linear evolution of  $\beta$ , obtained as a consequence of (40), is depicted in Figure 1.

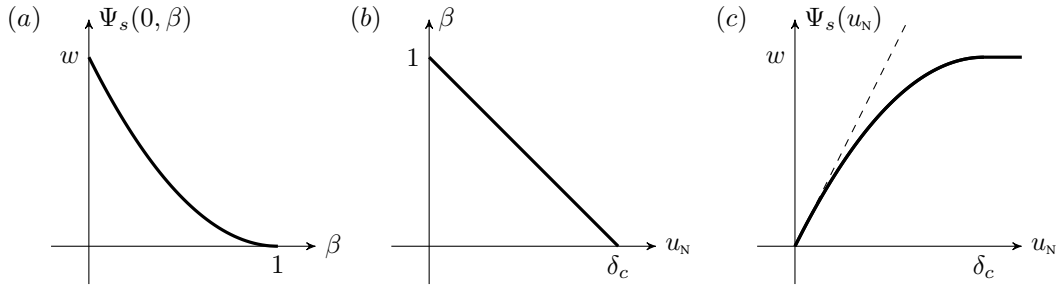


Figure 1: (a) The shape of the surface potential  $\Psi_s$  with respect to  $\beta$ . (b) The consequent linear evolution of  $\beta$  with  $u_N$ . (c) The shape of the surface potential  $\Psi_s$  with respect to  $u_N$ , where the initial slope is equivalent to the value of  $\sigma_c$ , and the final value is  $w$ .

The model (30) is now specified for a triangle law by

$$\begin{cases} \dot{\beta} = -\lambda, & \sigma_c(\delta_c(\beta - 1) + u_N) + A^r = \mu, & r_N + \beta\sigma_c = \nu, \\ -\nu \in N_{\mathbb{R}_+}(u_N), & -\mu \in N_{[0,1]}(\beta), & -\lambda \in N_{\mathbb{R}_+}(A^r). \end{cases} \quad (42)$$

Since  $\dot{\beta}$  is constrained to be non-positive, a smooth evolution of  $\beta$  starting with the initial value  $\beta = 1$  will result in  $\beta$  being less than 1. We will show that in this case the  $\mu_-$  condition written in (31) is redundant and can be dropped from the formulation. Let us assume that  $\beta = 1$  and  $\mu_- > 0$ . As  $\beta > 0$ ,  $\mu_+ = 0$  and  $\mu = -\mu_-$ . The second equation of (30) is then

$$\sigma_c u_N + A^r = -\mu_-. \quad (43)$$

As  $A^r$  and  $u_N$  are both constrained to be positive, (43) implies that  $\mu_- \leq 0$ , which contradicts our assumption. We conclude that  $\mu_-$  vanishes. Thus, the condition is redundant and is dropped from the model in the following, allowing us to write  $\mu = \mu_+$  and  $-\mu \in N_{\mathbb{R}_+}(\beta)$ .

This model in (42) can be written as a Mixed Linear Complementarity Systems (MLCS) given by

$$\begin{cases} \dot{\beta} = -\lambda, & \sigma_c(\delta_c(\beta - 1) + u_N) + A^r = \mu, & r_N + \beta\sigma_c = \nu, \\ 0 \leq \nu \perp u_N \geq 0, & 0 \leq \mu \perp \beta \geq 0, & 0 \leq \lambda \perp A^r \geq 0. \end{cases} \quad (44)$$

**Analytical expressions for an experiment with a given driven displacement** Let us assume for a while that  $u_N$  is a given function of time  $t$  given by the following piecewise linear function:

$$u_N(t) = \begin{cases} \frac{1}{2}t & \text{for } 0 \leq t < 1, \\ 1 - \frac{1}{2}t & \text{for } 1 \leq t < 2, \\ -1 + \frac{1}{2}t & \text{for } 2 \leq t, \end{cases} \quad (45)$$

where  $u_N$  is measured in mm and  $t$  in ms, and we choose  $\delta_c = 1$  mm and  $\sigma_c = \frac{1}{2}$  MPa. The time integration of the model described in (44) leads to the following piecewise linear response. We assume that the evolution is continuous.

- *First loading phase*  $0 \leq t < 1$

Since  $u_N(t) > 0$  for  $t > 0$ , the reaction force is  $r_N(t) = -\beta(t)\sigma_c$ . Let us assume that  $\beta(t) > 0$  for  $t \in [0, T_1)$ . We deduce that  $\mu(t) = 0$ . Let us note that  $A^r(t_0) = -\sigma_c(\delta_c(\beta_0 - 1) + u_N(0)) = 0$ . Let us assume that  $\lambda(t) = 0, t \in [0, \epsilon], \epsilon > 0$  or equivalently  $\dot{\beta}(t) = 0, t \in [0, \epsilon], \epsilon > 0$ . In that case, we get  $\dot{A}^r(t) = -\sigma_c v_N(t) < 0$  and then  $A^r(\epsilon) < 0$ , for  $\epsilon > 0$  which is impossible. Let us try with  $\dot{\beta}(t) < 0$ , then  $A^r(t) = 0$  and  $\beta(t) = 1 - \frac{u_N(t)}{\delta_c}$  and  $\dot{\beta}(t) = -\frac{v_N(t)}{\delta_c} < 0$ . Since  $\beta(1) = 1 - \frac{1}{2\delta_c} = \frac{1}{2} > 0$ , this is the only consistent solution for  $t \in [0, 1)$ .

- *Unloading phase*  $1 \leq t < 2$

Let us assume that  $\beta(t) > 0$  for  $t \in [1, 2)$  and  $\mu(t) = 0$ . Let us assume that  $\lambda(t) = 0, t \in [1, 2)$  or equivalently  $\dot{\beta}(t) = 0$ . In that case, we get  $\dot{A}^r(t) = -\sigma_c v_N(t) > 0$  and then  $A^r(t) = \frac{1}{4}(t - 1) > 0$ . This solution satisfies the complementarity condition up to  $t = 2$ .

- *Second loading phase*  $2 \leq t$

Let us assume that  $\beta(t) > 0$  for  $t \in [T_1, T_2)$  and  $\mu(t) = 0$ . Let us assume that  $\lambda(t) = 0, t \in [2, 2 + \epsilon], \epsilon > 0$  or equivalently  $\dot{\beta}(t) = 0$ . In that case, we get  $\dot{A}^r(t) = -\sigma_c v_N(t) < 0$  and then  $A^r(t) = -\frac{1}{2}\sigma_c(t - 2) + A^r(2) = -\frac{1}{4}(t - 3)$  which is positive for  $t < 3$ . For  $t \geq 3$ , the only possible solution of the complementarity leads to  $\dot{\beta}(t) = -\frac{v_N(t)}{\delta_c} < 0$  and  $A^r(t) = 0$ . The cohesion variable  $\beta$  is then  $\beta(t) = -\frac{1}{2}(t - 3) + \frac{1}{2}$  which is positive for  $t < 4$ . For  $t \geq 4$ , the solution is  $\beta(t) = 0$  and  $\mu(t) = \frac{1}{2}(u_N(t) - 1)$ .

The solution of this experiment is depicted in Figure 2.

**Remark 3.** Let us note that we need to derive the second term of (44) to get a closed form solution. This means that the evolution variational inequality is of relative degree at least 1.

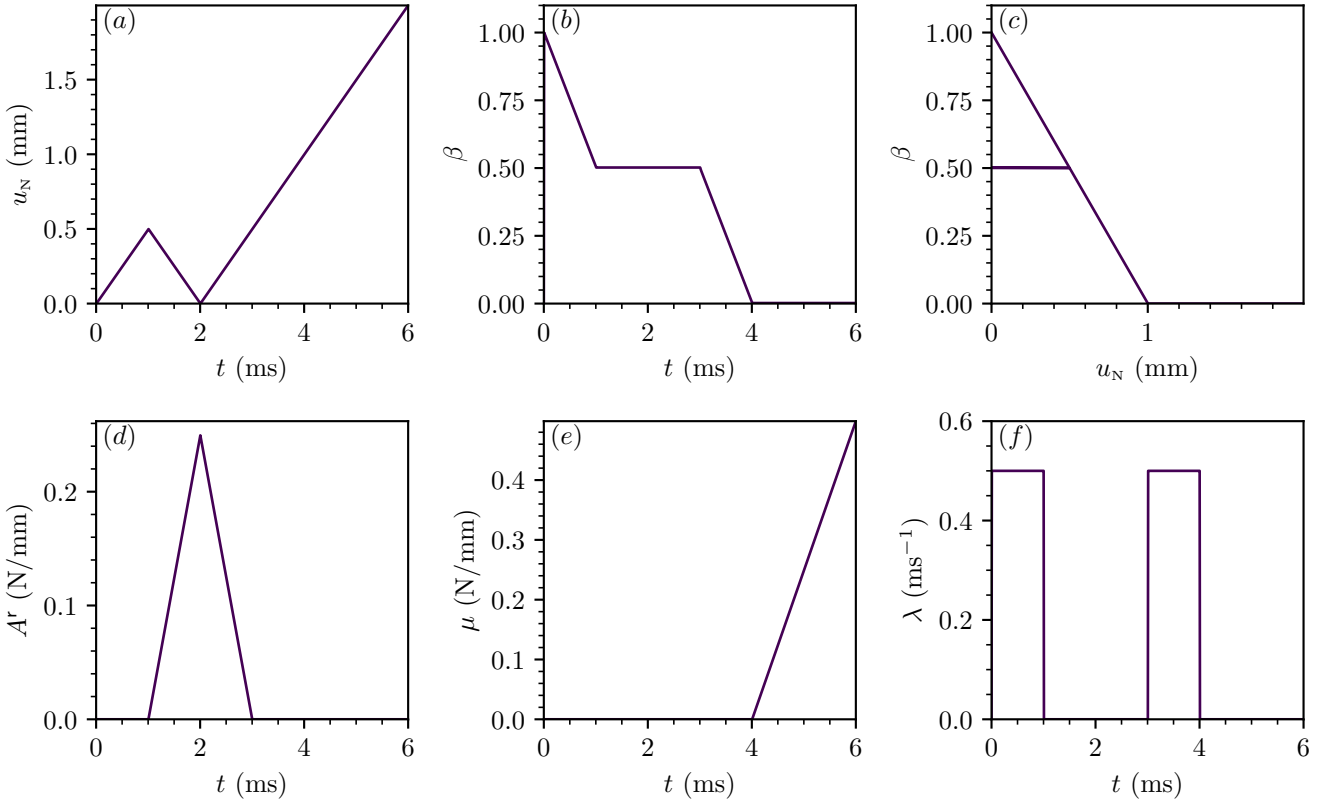


Figure 2: Illustration of the extrinsic cohesive law with a linear evolution of cohesion. (a) The displacement  $u_N$  as a function of time  $t$ . (b) The cohesion  $\beta$  as a function of time  $t$ . (c) The cohesion  $\beta$  as a function of displacement  $u_N$ . (d) The thermodynamic driving force  $A^r$  as a function of time. (e) The slack variable  $\mu$  as a function of time  $t$ . (f) The slack variable  $\lambda$  as a function of time  $t$ .

We observe in Figure 2 that the model behaves correctly, with  $\beta$  only changing as the crack opens  $v_N > 0$ , and no change in  $\beta$  during reloading until  $u_N$  exceeds its previous maximum value. Once the interface cohesion is fully eliminated we observe no further change in  $\beta$ .

**Remark 4.** *Other types of smoother cohesion evolution behaviours are possible, for examples laws modelled after that proposed in Michel and Suquet (1994).*

**Remark 5.** *We note in particular that other unloading behaviours are possible within the non-smooth mechanics framework. Rather than the horizontal unload-reload behaviour exhibited in our model, Talon and Curnier (2003) proposed a model where the unload-reload behaviour is vertical. This behaviour arises as they treat adhesion as a phenomenon featuring thin filaments that immediately crumple under unloading, and thus cannot exert any force whatsoever. However, we view cohesion as the material providing a force that acts to close the crack, and unloading changes nothing about the underlying material state that would cause this force to change. We note that these two views are not mutually exclusive, as they model subtly different phenomena (adhesion vs cohesion).*

### 3 Non-smooth elasto-dynamics of finite-dimensional systems

We now extend our model to consider bodies with finite numbers of degrees of freedom, to which are attached masses, stiffnesses and external forces. These degrees of freedom may or may not be associated with cohesive zones. We also consider the dynamic interaction of multiple bodies via the formulation of an impact law for the system.

#### 3.1 Finite-dimensional systems via space-discretisation

Let us consider a finite-dimensional model of a linear elastic mechanical system, potentially after a space-discretisation by the finite element method. Let us note by  $u \in \mathbb{R}^n$  the displacements of the system and  $v = \dot{u}$  the velocity. Starting from the principle of virtual power (7), the equilibrium equation can be written as

$$M\dot{v} + K u = F; \quad \dot{u} = v, \tag{46}$$

where  $M \in \mathbb{R}^{n \times n}$  is the mass matrix, assumed to be symmetric positive definite,  $K \in \mathbb{R}^{n \times n}$  is the structural symmetric semi-definite positive stiffness matrix and  $F \in \mathbb{R}^n$  is the external applied force.

Let us now add that the cohesive zone is applied on a finite set of cohesive contact points labelled by  $\alpha \in \llbracket 1, m \rrbracket$ . In the case of small perturbations, the local displacements at contact  $u_N = \text{col}(u_N^\alpha, \alpha \in \llbracket 1, m \rrbracket)$  are related to the displacements  $u$  by a linear relation written as

$$u_N = H u + b, \tag{47}$$

where  $H \in \mathbb{R}^{m \times n}$  and  $b \in \mathbb{R}^m$ . Collecting all variables at contact in the same way ( $x = \text{col}(x^\alpha, \alpha \in \llbracket 1, m \rrbracket)$ ), the equilibrium equations of the system are given by

$$\begin{cases} M\dot{v} + K u = F + H^\top S r_N, & \dot{u} = v, & \dot{\beta} = -\lambda, \\ u_N = H u + b, & r_N^c = \beta \sigma_c, \\ w f'(\beta) + \sigma_c u_N + A^r = \mu, & r_N + r_N^c = \nu, \\ -\nu \in N_{\mathbb{R}_+}(u_N), & -\mu \in N_{\mathbb{R}_+}(\beta), & -\lambda \in N_{\mathbb{R}_+}(A^r), \end{cases} \tag{48}$$

where  $S \in \mathbb{R}^{m \times m}$  is a diagonal matrix that contains the tributary area of each cohesive zone node after space-discretisation of the interface. For the sake of simplicity, we assume that  $\sigma_c$ ,  $w$  and  $f$  do not depend on  $\alpha$ , but this can be straightforwardly extended.

#### 3.2 Non-smooth dynamics and impacts

In the presence of unilateral contacts, solutions of finite-dimensional dynamical systems with a regular mass matrix (with finite masses associated with all degrees of freedom) exhibit jumps in velocities. In this context, the non-smooth dynamics must be carefully treated to obtain a consistent time-discretisation (Moreau, 1999). To this end, the equations of motion of a discrete (finite-dimensional) mechanical system, and the relation with contact variables are written in terms of differential measures by

$$\begin{cases} M dv + K u dt = F dt + H^\top di_N, \\ \dot{u} = v, \end{cases} \tag{49}$$

where  $dv$  is the differential measure associated with the velocity  $v$ , assumed to be a bounded value function, and  $di_N$  is the measure of the reaction at the contact. For the cohesive zone model, several further assumptions are made:

- We assume that the reaction due to cohesion force  $r_N^c$  is bounded. In other words, the corresponding impulse does not contain atoms (Dirac measures);
- We assume that  $\beta$  and  $A^r$  are absolutely continuous functions of time. Since the evolution of the cohesion variable is governed by the displacement  $u_N$  that is assumed to be absolutely continuous in time, we assume the same regularity for  $\beta$  and  $A^r$ .

The reaction at the contact can then be decomposed into the “contact impulse”  $dp_N$ , and the contribution of the cohesive forces by

$$di_N = S dp_N - S\sigma_c\beta dt. \quad (50)$$

When the interface is completely broken, we want to retrieve a contact law with impact. We choose in this work Moreau’s impact law

$$0 \leq dp_N \perp v_N^+ + ev_N^- \geq 0 \text{ if } u_N \leq 0, \text{ else } dp_N = 0, \quad (51)$$

where  $e$  is the Newton coefficient of restitution. In terms of normal cone inclusion, this is equivalent to

$$-dp_N \in N_{T_{\mathbb{R}_+}(u_N)}(v_N^+ + ev_N^-), \text{ or equivalently, } -(di_N + S\sigma_c\beta dt) \in N_{T_{\mathbb{R}_+}(u_N)}(v_N^+ + ev_N^-), \quad (52)$$

where  $T_{\mathbb{R}_+}$  is the tangent cone of the set  $\mathbb{R}_+$ .

**Remark 6.** *The inclusion  $-dp_N \in N_{T_{\mathbb{R}_+}(u_N)}(v_N^+ + ev_N^-)$  deals with the impact and the constraints at the velocity level. When  $u_N(t) = 0$ , this inclusion imposes that  $v_N^+(t) \geq 0$  and then  $u_N(t + \epsilon) \geq 0$  for  $\epsilon > 0$ . This result is formalised in Moreau’s viability lemma (Moreau, 1999). The inequality  $u_N \geq 0$  is not explicitly written since it is satisfied if (51) is satisfied and  $u_N(t_0) \geq 0$ .*

Thus, we can write the full set of equations for the system as

$$\left\{ \begin{array}{l} M dv + Ku dt = F dt + H^\top (S dp_N - S\sigma_c\beta dt), \quad \dot{u} = v, \quad \dot{\beta} = -\lambda, \\ u_N = Hu + b, \quad v_N = Hv, \quad wf'(\beta) + \sigma_c u_N + A^r = \mu, \\ -\mu \in N_{\mathbb{R}_+}(\beta), \\ -\lambda \in N_{\mathbb{R}_+}(A^r), \\ -dp_N \in N_{T_{\mathbb{R}_+}(u_N)}(v_N^+ + ev_N^-). \end{array} \right. \quad (53)$$

In complementarity terms, we write the model as

$$\left\{ \begin{array}{l} M dv + Ku dt = F dt + H^\top (S dp_N - S\sigma_c\beta dt), \\ \dot{u} = v, \\ \dot{\beta} = -\lambda, \\ u_N = Hu + b, \\ v_N = Hv, \\ wf'(\beta) + \sigma_c u_N + A^r = \mu, \\ 0 \leq \mu \perp \beta \geq 0, \\ 0 \leq A^r \perp \lambda \geq 0, \\ 0 \leq dp_N \perp v_N^+ + ev_N^- \geq 0 \text{ if } u_N \leq 0, \text{ else } dp_N = 0. \end{array} \right. \quad (54)$$

The formulation of the dynamics of the problem with impact and a cohesive zone model is rather different from what is proposed in Acary and Monerie (2006). In (53), the cohesion impulse measure  $-\sigma_c S\beta dt$  is assumed to have only a density with respect to the Lebesgue measure. Furthermore, it is decoupled from the contact impulse measure  $dp_N$  in the formulation of the constitutive laws of the interface. In other words, the cohesive reaction force is driven by  $u_N$  and the contact impulse measure by  $v_N^+ + ev_N^-$ .

## 4 Numerical time integration

We now specify the time-discretisation of the system, and show that it can be rearranged to a linear complementarity problem. We then demonstrate that this problem is well-posed, and that the resulting discrete energy balance is dissipative.

## 4.1 Principles of the time integration scheme

The time-integration scheme is based on the same principle as the Moreau–Jean scheme (Acary and Brogliato, 2008; Jean, 1999; Jean and Moreau, 1992; Moreau, 1999) for contact dynamics. For the impulsive terms, the measure of the time interval  $(k, k+1]$  is kept as a primary unknown:

$$p_{N,k,k+1} \approx dp_N((k, k+1]) = \int_{(k,k+1]} dp_N \text{ and } i_{N,k,k+1} \approx di_N((k, k+1]) = \int_{(k,k+1]} di_N. \quad (55)$$

All the continuous or bounded value terms are approximated with a  $\theta$ -method by

$$\int_{t_k}^{t_{k+1}} x(t) dt \approx hx_{k+\theta}, \quad (56)$$

using the notation  $x_{k+\theta} = \theta x_k + (1-\theta)x_{k+1}$  with  $\theta \in [0, 1]$ . For the cohesive reaction force that is assumed to be bounded, we have

$$\int_{(k,k+1]} di_N = S \int_{(k,k+1]} dp_N - S \int_{t_k}^{t_{k+1}} \sigma_c \beta dt, \quad (57)$$

that is approximated by

$$i_{N,k,k+1} = Sp_{N,k,k+1} - h\sigma_c S\beta_{k+\theta}. \quad (58)$$

The last equation of (54) is discretised as follows:

$$0 \leq p_{N,k,k+1} \perp v_{N,k+1} + ev_{N,k} \geq 0 \text{ if } \tilde{u}_{N,k} \leq 0, \text{ else } p_{N,k,k+1} = 0, \quad (59)$$

where a conditional statement determining whether contact occurs is defined by an approximation of the displacement usually defined as :

$$\tilde{u}_{n,k} = u_{N,k} + \frac{h}{2}v_{N,k}. \quad (60)$$

In the following, we consider the index set  $I_k = \{\alpha, \tilde{u}_{N,k}^\alpha \leq 0\}$  and the following compact notation  $p_{N,k,k+1} = \text{col}(p_{N,k,k+1}^\alpha, \alpha \in I_k)$ ,  $v_{N,k+1} = \text{col}(v_{N,k+1}^\alpha, \alpha \in I_k)$ ,  $\bar{H} = \text{row}(H_{I_k}, \alpha \in I_k) = H_{I_k}$ . Following this principle, the time-stepping scheme is written as follows:

$$\left\{ \begin{array}{l} M(v_{k+1} - v_k) + hK u_{k+\theta} = hF_{k+\theta} - h\sigma_c H^\top S\beta_{k+\theta} + \bar{H}^\top Sp_{N,k,k+1}, \\ u_{k+1} = u_k + hv_{k+\theta}, \\ \beta_{k+1} - \beta_k = -h\lambda_{k+1}, \\ u_{N,k+1} = Hu_{k+1} + b_{k+1}, \\ v_{N,k+1} = \bar{H}v_{k+1}, \\ wf'(\beta_{k+1}) + \sigma_c u_{N,k+1} + A^r_{k+1} = \mu_{k+1}, \\ 0 \leq \beta_{k+1} \perp \mu_{k+1} \geq 0, \\ 0 \leq A^r_{k+1} \perp \lambda_{k+1} \geq 0, \\ 0 \leq p_{N,k,k+1} \perp v_{N,k+1} + ev_{N,k} \geq 0. \end{array} \right. \quad (61)$$

The problem (61) amounts to solving a special type of finite-dimensional variational inequality at each time step, namely a Mixed Complementarity Problem.

**Discrete LCP for the triangular law.** The only non-linear term in the formulation of the complementarity system is due to  $f'$ . In the following, we show that if  $f'$  is linear, the problem (61) reduces to a Linear Complementarity System  $\text{LCP}(L, q)$  defined by

$$\left\{ \begin{array}{l} w = Lz + q, \\ 0 \leq w \perp z \geq 0. \end{array} \right. \quad (62)$$

Substituting the triangle law into (61), we finally obtain the discretisation:

$$\left\{ \begin{array}{l} M(v_{k+1} - v_k) + hK u_{k+\theta} = hF_{k+\theta} - h\sigma_c H^\top S \beta_{k+\theta} + \bar{H}^\top S p_{N,k,k+1}, \\ u_{k+1} = u_k + h v_{k+\theta}, \\ \beta_{k+1} - \beta_k = -h \lambda_{k+1}, \\ u_{N,k+1} = H u_{k+1} + b_{k+1}, \\ v_{N,k+1} = \bar{H} v_{k+1}, \\ \sigma_c \delta_c (\beta_{k+1} - 1) + \sigma_c u_{N,k+1} + A^r_{k+1} = \mu_{k+1}, \\ 0 \leq \beta_{k+1} \perp \mu_{k+1} \geq 0, \\ 0 \leq A^r_{k+1} \perp \lambda_{k+1} \geq 0, \\ 0 \leq p_{N,k,k+1} \perp v_{N,k+1} + e v_{N,k} \geq 0. \end{array} \right. \quad (63)$$

Now, if we expand the first line with the appropriate  $\theta$ -method substitutions, we arrive at

$$M(v_{k+1} - v_k) + hK \left( u_k + h\theta [(1-\theta)v_k + \theta v_{k+1}] \right) = h [(1-\theta)F_k + \theta F_{k+1}] - h\sigma_c H^\top S [(1-\theta)\beta_k + \theta\beta_{k+1}] + \bar{H}^\top S p_{N,k,k+1}. \quad (64)$$

We denote the augmented mass matrix as  $\hat{M} = M + h^2\theta^2 K$  and the free impulse (without the contribution of the cohesive zone model)  $\hat{i}_{k,k+1} = M v_k - hK (u_k + h\theta(1-\theta)v_k) + h [(1-\theta)F_k + \theta F_{k+1}]$ . Thus, the velocities can be determined by

$$v_{k+1} = \hat{M}^{-1} \left[ \hat{i}_{k,k+1} - h\sigma_c H^\top S [(1-\theta)\beta_k + \theta\beta_{k+1}] + \bar{H}^\top S p_{N,k,k+1} \right], \quad (65)$$

and then

$$\begin{aligned} v_{N,k+1} &= \bar{H} \hat{M}^{-1} \hat{i}_{k,k+1} - h\sigma_c \bar{H} \hat{M}^{-1} H^\top S [(1-\theta)\beta_k + \theta\beta_{k+1}] + \bar{H} \hat{M}^{-1} \bar{H}^\top S p_{N,k,k+1}, \\ &= \bar{H} \hat{M}^{-1} \hat{i}_{k,k+1} + h\sigma_c V S (\theta h \lambda_{k+1} - \beta_k) + W S p_{N,k,k+1}, \end{aligned} \quad (66)$$

where  $W = \bar{H} \hat{M}^{-1} \bar{H}^\top$  is the Delassus matrix reduced to active contacts and  $V = \bar{H} \hat{M}^{-1} H^\top$ . When necessary, we modify the augmented mass matrix  $\hat{M}$  and the free impulse  $\hat{i}$  to take into account Dirichlet boundary conditions. In the same way as the velocity, we expand  $A^r_{k+1} = \mu_{k+1} - \sigma_c \delta_c (\beta_{k+1} - \mathbf{1}) - \sigma_c u_{N,k+1}$  where  $\mathbf{1}$  represents a vector of ones, using the expression of  $u_{N,k+1}$  for all cohesive points:

$$\begin{aligned} u_{N,k+1} &= u_{N,k} + h(1-\theta)H v_k + h\theta H v_{k+1} + b_{k+1}, \\ &= u_{N,k} + h(1-\theta)H v_k + h\theta H \hat{M}^{-1} \left[ \hat{i}_{k,k+1} + h\sigma_c H^\top S (\theta h \lambda_{k+1} - \beta_k) + \bar{H}^\top S p_{N,k,k+1} \right] + b_{k+1}, \\ &= h^2\theta^2 \sigma_c U S h \lambda_{k+1} + h\theta V^\top S p_{N,k,k+1} + u_{N,k} + h(1-\theta)H v_k + h\theta H \hat{M}^{-1} \hat{i}_{k,k+1} - h^2\theta \sigma_c U S \beta_k + b_{k+1}, \end{aligned} \quad (67)$$

where  $U = H \hat{M}^{-1} H^\top$  is the complete Delassus matrix. We obtain

$$\begin{aligned} A^r_{k+1} &= \mu_{k+1} + \sigma_c (\delta_c I - h^2\theta^2 \sigma_c U S) h \lambda_{k+1} - h\theta \sigma_c V^\top S p_{N,k,k+1} \\ &\quad - \sigma_c \left( \delta_c (\beta_k - \mathbf{1}) + u_{N,k} + h(1-\theta)H v_k + h\theta H \hat{M}^{-1} \hat{i}_{k,k+1} - h^2\theta \sigma_c U S \beta_k + b_{k+1} \right). \end{aligned} \quad (68)$$

We can now formulate an LCP with three variable pairs,  $(A, h\lambda)$ ,  $(\beta, \mu)$  and  $(v_N^+ + e v_N^-, p_N)$ , noting that the unusual formulation of the third variable pair is required by the complementarity condition. In the most general case of multiple cohesive zones with boundary conditions enforced, the LCP( $L, q$ ) is defined by

$$\begin{aligned} L &= \begin{bmatrix} \mathbf{0} & -I & \mathbf{0} \\ I & \sigma_c (\delta_c I - h^2\theta^2 \sigma_c U S) & -h\theta \sigma_c V^\top S \\ \mathbf{0} & h\theta \sigma_c V S & W S \end{bmatrix}, \\ q &= \begin{bmatrix} \beta_k \\ -\sigma_c \left( \delta_c (\beta_k - \mathbf{1}) + u_{N,k} + h(1-\theta)H v_k + h\theta H \hat{M}^{-1} \hat{i}_{k,k+1} - h^2\theta \sigma_c U S \beta_k + b_{k+1} \right) \\ \bar{H} \hat{M}^{-1} \hat{i}_{k,k+1} - h\sigma_c V S \beta_k + e v_{N,k} \end{bmatrix}, \end{aligned} \quad (69)$$

where  $\mathbf{0}$  represents a matrix of zeroes, and  $I$  is the identity matrix. The LCP is solved for the following complementarity variables:

$$w = \begin{bmatrix} \beta_{k+1} \\ A^r_{k+1} \\ v_{N,k+1} + e v_{N,k} \end{bmatrix}, \quad z = \begin{bmatrix} \mu_{k+1} \\ h \lambda_{k+1} \\ p_{N,k,k+1} \end{bmatrix}, \quad (70)$$

where all of the cohesive zone variables should be understood as vectors. It is possible to straightforwardly generalise to each cohesive zone possessing its own values of the material parameters, in which case the material parameters can be treated as vectors.

**Remark 7.** *The choice of  $h\lambda_{k+1}$  as an unknown of the LCP, rather than  $\lambda_{k+1}$ , is made to ensure that  $L$  does not degenerate in the limit as  $h \rightarrow 0$ . This is related to the fact that  $\lambda$ , and hence  $\beta$  may jump at a given instant (see Figure 2).*

## 4.2 Well-posedness of the discrete LCP

We wish to demonstrate that the system (69) exhibits correct behaviour for sufficiently small time steps, *i.e.* that it has a unique solution for the state variables, and hence will reliably resolve the system numerically without introducing spurious and unphysical solution jumps. Let us start by formulating the main assumption:

**Assumption 1.** *The time step  $h$  is chosen such that  $\delta_c I - h^2 \theta^2 \sigma_c U S$  is positive definite.*

Now, we prove a proposition that the system is well-posed:

**Proposition 1.** *Under Assumption 1, the LCP( $L, q$ ) defined by (69) has a solution. The solution is unique for  $\beta_{k+1}$  and  $\lambda_{k+1}$  and  $v_{N,k+1}$ . For  $\beta_k > 0$ , the solution is also unique for  $A^T_{k+1}$  and  $\mu_{k+1}$ .*

We start by proving that  $L$  is a semi-positive definite matrix for  $h$  satisfying Assumption 1. Proving this property for  $L$  amounts to proving that  $\frac{1}{2} (L + L^\top)$  given by

$$\frac{1}{2} (L + L^\top) = \begin{bmatrix} \mathbf{0} & \mathbf{0} & \mathbf{0} \\ \mathbf{0} & \sigma_c (\delta_c I - h^2 \theta^2 \sigma_c U S) & \mathbf{0} \\ \mathbf{0} & \mathbf{0} & W S \end{bmatrix}, \quad (71)$$

is also a positive semi-definite matrix. Since  $M$  is a positive definite matrix, the matrices  $W$  and  $U$  are semi-positive definite matrices. Therefore, we can conclude that  $L$  is a semi-definite positive matrix. From Theorem 3.1.2 in Cottle et al. (2009), if the LCP( $L, q$ ), with a semi-definite positive matrix  $L$ , is feasible, then it is solvable. The feasibility conditions for a LCP are given by

$$Lz + q \geq 0 \text{ and } z \geq 0, \quad (72)$$

and in the case of LCP( $L, q$ ),

$$\begin{cases} z_1 \geq 0, z_2 \geq 0, z_3 \geq 0, \\ -z_2 + \beta_k \geq 0, \\ z_1 + \sigma_c (\delta_c I - h^2 \theta^2 \sigma_c U S) z_2 - h \theta \sigma_c S V^\top z_3 + q_2 \geq 0, \\ h \theta \sigma_c V S z_2 + W S z_3 + q_3 \geq 0. \end{cases} \quad (73)$$

Rearranging the inequalities, we obtain

$$\begin{cases} 0 \leq z_2 \leq \beta_k, \\ z_1 \geq 0, z_1 \geq -\sigma_c (\delta_c I - h^2 \theta^2 \sigma_c U S) z_2 + h \theta \sigma_c S V^\top z_3 - q_2, \\ z_3 \geq 0, W S z_3 \geq -h \theta \sigma_c V S z_2 - q_3. \end{cases} \quad (74)$$

Since  $\beta_k \geq 0$ , the first inequality is feasible for  $z_2$ . Let us search for a feasible point  $z^*$  such that  $z_2^* = 0$ . We must check that the following inequalities are feasible for  $z_1^*$  and  $z_3^*$ :

$$\begin{cases} z_1^* \geq h \theta \sigma_c S V^\top z_3^* - q_2, z_1^* \geq 0, \\ W S z_3^* + q_3 \geq 0, z_3^* \geq 0. \end{cases} \quad (75)$$

Let us consider the following convex quadratic program:

$$\begin{aligned} \min_{z_3} \quad & \frac{1}{2} z_3^\top W S z_3 + z_3^\top q_3, \\ & z_3 \geq 0. \end{aligned} \quad (76)$$

A solution  $z_3^*$  of (76) exists and satisfies the optimality conditions:

$$w_3^* = W S z_3^* + q_3 \geq 0, z_3^* \geq 0, w_3^{*\top} z_3^* = 0. \quad (77)$$

Finally, let us choose  $z_1^* = \max(0, h\theta\sigma_c S V^\top z_3^* - q_2)$ , which satisfies the relevant inequalities. We have proved that the point  $z = \text{col}(z_1^*, 0, z_3^*)$  is a feasible point of the inequalities (73). The LCP( $L, q$ ) is feasible and thus solvable.

For the uniqueness of the solution, we use the characterisation of the solutions of LCP( $L, q$ ), denoted by SOL( $L, q$ ), when  $L$  is a semi-positive definite matrix (Cottle et al., 2009, Theorem 3.1.7) as a polyhedral set defined by

$$\text{SOL}(L, q) = \left\{ z \mid z \geq 0, Lz + q \geq 0, q^\top(z - \bar{z}) = 0, (L + L^\top)(z - \bar{z}) = 0 \right\}, \quad (78)$$

where  $\bar{z}$  is an arbitrary solution. In our case, the condition  $(L + L^\top)(z - \bar{z}) = 0$  yields

$$\begin{cases} \sigma_c (\delta_c I - h^2 \theta^2 \sigma_c U S) (z_2 - \bar{z}_2) = 0, \\ W S (z_3 - \bar{z}_3) = 0. \end{cases} \quad (79)$$

Under Assumption 1,  $\delta_c I - h^2 \theta^2 \sigma_c U S$  has full-rank. We get that  $z_2$ , and hence  $h\lambda_{k+1}$  is unique. Since  $\beta_{k+1} = \beta_k - h\lambda_{k+1}$ ,  $\beta_{k+1}$  is also unique. From  $w_3 - \bar{w}_3 = h\theta\sigma_c V S (z_2 - \bar{z}_2) + W S (z_3 - \bar{z}_3) = 0$ , we conclude that  $w_3$  is unique and therefore  $v_{N,k+1}$  is also unique. Furthermore,  $(z_3 - \bar{z}_3)$  is in the kernel of  $W$  and then of  $\bar{H}^\top$ , so we have also  $\bar{H}^\top(z_3 - \bar{z}_3) = 0$ .

From the condition,  $q^\top(z - \bar{z}) = 0$ , we obtain

$$\beta_k(z_1 - \bar{z}_1) + \left( \bar{H} \hat{M}^{-1} \left( \hat{i}_{k,k+1} - h H^\top S \sigma_c \beta_k \right) + e v_{N,k} \right)^\top (z_3 - \bar{z}_3) = 0, \quad (80)$$

since  $z_2 - \bar{z}_2 = 0$ . Since  $v_{N,k} = \bar{H} v_k$ , we have the following simplification:

$$\left( \hat{M}^{-1} \left( \hat{i}_{k,k+1} - h(1-\theta)\sigma_c H^\top S \beta_k \right) + e v_k \right)^\top \bar{H}^\top (z_3 - \bar{z}_3) = 0, \quad (81)$$

since  $\bar{H}^\top(z_3 - \bar{z}_3) = 0$ , and then

$$\beta_k(z_1 - \bar{z}_1) = 0. \quad (82)$$

For  $\beta_k > 0$ ,  $z_1$ , hence  $\mu_{k+1}$  is unique. Using that the linear relations  $A_{k+1}^r = \mu_{k+1} - \sigma_c \delta_c (\beta_{k+1} - 1) + \sigma_c u_{N,k+1}$  and  $u_{N,k+1} = u_{N,k} + h v_{N,k+\theta}$ , we conclude that  $A_{k+1}^r$  is unique if  $\beta_k > 0$ .

**Corollary 1.** *Under Assumption 1, the solution of the problem (63) exists and is unique for the variables  $(v_{k+1}, u_{k+1}, \beta_{k+1}, \lambda_{k+1})$  for a sufficiently small time step  $h$ .*

The uniqueness of  $\beta_{k+1}$  comes from Proposition 1. For the uniqueness of  $v_{k+1}$ , let us consider two solutions  $\hat{v}_{k+1}, \hat{\beta}_{k+1}, \hat{p}_{N,k,k+1}$  and  $\bar{v}_{k+1}, \bar{\beta}_{k+1}, \bar{p}_{N,k,k+1}$ , from (65), we get

$$\hat{v}_{k+1} - \bar{v}_{k+1} = \hat{M}^{-1} \left[ -h\theta\sigma_c H^\top S (\hat{\beta}_{k+1} - \bar{\beta}_{k+1}) + \bar{H}^\top S (\hat{p}_{N,k,k+1} - \bar{p}_{N,k,k+1}) \right]. \quad (83)$$

Since  $\hat{p}_{N,k,k+1} - \bar{p}_{N,k,k+1}$  is in the kernel of  $\bar{H}^\top$  and  $\hat{\beta}_{k+1} - \bar{\beta}_{k+1} = 0$ , we can conclude that  $v_{k+1}$  is unique, and the integration rule  $u_{k+1} = u_k + h v_{k+\theta}$  implies the uniqueness of  $u_{k+1}$ .

**Corollary 2** (Convex optimisation problem). *Under Assumption 1, the LCP( $L, q$ ) is equivalent to the following convex quadratic problem:*

$$\begin{aligned} \min_{h\lambda_{k+1}, p_{N,k,k+1}, \mu_{k+1}} \quad & \frac{1}{2} \begin{bmatrix} h\lambda_{k+1} \\ p_{N,k,k+1} \end{bmatrix}^\top \begin{bmatrix} \sigma_c (\delta_c I - h^2 \theta^2 \sigma_c U S) & \mathbf{0} \\ \mathbf{0} & W S \end{bmatrix} \begin{bmatrix} h\lambda_{k+1} \\ p_{N,k,k+1} \end{bmatrix} + q^\top \begin{bmatrix} \mu_{k+1} \\ h\lambda_{k+1} \\ p_{N,k,k+1} \end{bmatrix}, \\ \text{subject to} \quad & \mu_{k+1} \geq 0, h\lambda_{k+1} \geq 0, p_{N,k,k+1} \geq 0, \\ & -h\lambda_{k+1} + q_1 \geq 0, \\ & \mu_{k+1} + \sigma_c (\delta_c I - h^2 \theta^2 \sigma_c U S) h\lambda_{k+1} - h\theta\sigma_c V^\top S p_{N,k,k+1} + q_2 \geq 0, \\ & h\theta\sigma_c V S h\lambda_{k+1} + W S p_{N,k,k+1} + q_3 \geq 0. \end{aligned} \quad (84)$$

The following remarks and comments can be made:

- The condition on the size of the time step is not an onerous one in practice since it is based on the condition that  $\delta_c I - h^2 \theta^2 \sigma_c U S$  is positive definite in which  $h$  only appears as  $h^2$ . In most finite elements applications,  $H$  is assumed to be full-rank. In that case,  $p_{N,k,k+1}$  is also unique. The possible non-uniqueness of  $\mu_{k+1}$  and  $A_{k+1}^r$  when  $\beta_k = 0$  comes from the fact that we impose two redundant constraints  $\beta_{k+1} \geq 0$  and  $\beta_{k+1} \leq 0$  related to  $\beta \geq 0$  and  $\dot{\beta} \leq 0$ . In practice, this is harmless since it does not influence the state variables  $(v_{k+1}, u_{k+1}, \beta_{k+1})$ .

- It is important to note that the LCP becomes infeasible if  $\beta_k < 0$ . While in principle the constraints act to enforce a  $\beta_k = 0$  condition, in practice due to the finite numerical precision of the solution at each step, the condition can be violated. In this case, the solution of the LCP can fail in turn. As such, when the value of  $\beta_k$  is near the machine accuracy, we set  $\beta_{k+1}$  to 0 and  $\mu_{k+1}$  is given by the equation (68). We reduce the corresponding contact to a simple unilateral contact with impact LCP solving only for  $v_{N,k+1}, p_{N,k,k+1}$ . We note that this schema is also effective numerically, as by decreasing the size of the LCP, we speed up its solution.
- The convex minimisation problem has no straightforward mechanical meaning. A future goal would be to express a convex minimisation problem in the spirit of the variational approach to fracture (Bourdin et al., 2008). This is beyond the scope of the paper and left to further investigations.
- In practice, the LCP( $L, q$ ) can be solved by pivoting techniques for LCPs (such as Lemke's algorithm) or other methods such as interior point methods, taking advantage of the convex minimisation problem (Nocedal and Wright, 1999; Wright, 1996) (see also Acary and Brogliato (2008, Chapter 9) in the context of non-smooth mechanics).

### 4.3 Discrete energy balance

In this section, we show that the discrete energy balance is satisfied by the proposed time-stepping scheme. Starting from the energy balance in the non-impulsive case in (36), we need to adapt the definition of the energy balance when impacts occur, as can be the case with finite masses. Starting from the equation of motion given in (49) and multiplying by  $\frac{1}{2}(v^+ + v^-)$ , we get

$$\frac{1}{2}(v^+ + v^-)^\top M dv + \frac{1}{2}(v^+ + v^-)^\top K u dt = \frac{1}{2}(v^+ + v^-)^\top F dt + \frac{1}{2}(v^+ + v^-)^\top H^\top S dp_N - \frac{1}{2}(v^+ + v^-)^\top H^\top \sigma_c S \beta dt, \quad (85)$$

Since  $v^+ dt = v^- dt = v dt$  and  $M$  and  $K$  are symmetric matrices, we obtain

$$d\left(\frac{1}{2}v^\top M v\right) + d\left(\frac{1}{2}u^\top K u\right) = F^\top v dt - (Hv)^\top \sigma_c S \beta dt + \frac{1}{2}\left[H(v^+ + v^-)\right]^\top S dp_N. \quad (86)$$

With the standard definition of the kinetic energy  $K$  and strain potential energy  $U$  in the space-discretised case, we obtain

$$dK + dU = F^\top v dt - (Hv)^\top \sigma_c S \beta dt + \frac{1}{2}\left[H(v^+ + v^-)\right]^\top S dp_N = v^\top F dt - v_N^\top \sigma_c S \beta dt + \frac{1}{2}(v_N^+ + v_N^-)^\top S dp_N. \quad (87)$$

With the space-discretised version of the fracture energy given in (38)

$$G = \int v_N^\top \sigma_c S \beta dt, \quad (88)$$

we obtain the equivalent energy balance for the space-discretised system:

$$dK + dU + dG = v^\top F dt + \frac{1}{2}(v_N^+ + v_N^-)^\top S dp_N. \quad (89)$$

By integrating this latter relation over a time interval  $(t_1, t_2]$  and defining the total energy of the system as  $T = K + U + G$ , we obtain the incremental energy balance:

$$\Delta T = T^+(t_2) - T^-(t_1) = W_{\text{ext}} + W_{\text{impact}}, \quad (90)$$

where the work of external forces and impact are given by

$$W_{\text{ext}} = \int_{t_1}^{t_2} v^\top F dt, \text{ and } W_{\text{impact}} = \int_{(t_1, t_2]} \frac{1}{2}(v_N^+ + v_N^-)^\top S dp_N. \quad (91)$$

Using the constitutive law for the impact equation (52), it is shown (Acary, 2016) that as the work of impact dissipates energy, then

$$\Delta T = T^+(t_2) - T^-(t_1) - W_{\text{ext}} = W_{\text{impact}} \leq 0. \quad (92)$$

Let us now show that an equivalent incremental energy balance is also satisfied by the time-stepping method. Following the same method as in Acary (2016), we derive the following incremental energy balance for the  $\theta$ -method:

$$\Delta K + \Delta U = \left(\frac{1}{2} - \theta\right) \left[ \|v_{k+1} - v_k\|_M^2 + \|(u_{k+1} - u_k)\|_K^2 \right] + hv_{k+\theta}^\top F_{k+\theta} - hv_{N,k+\theta}^\top \sigma_c S \beta_{k+\theta} + v_{N,k+\theta}^\top S p_{N,k,k+1}, \quad (93)$$

where  $\|v\|_M^2 = v^\top M v$  and  $\|u\|_K^2 = u^\top K u$ . Let us define the discrete approximation of the work done by the external forces and the impact term within the step by

$$W_{\text{ext},k+1} = h v_{k+\theta}^\top F_{k+\theta} \approx \int_{t_k}^{t_{k+1}} F v \, dt, \text{ and } W_{\text{impact},k+1} = v_{N,k+\theta}^\top S p_{N,k,k+1}, \quad (94)$$

and the discrete approximation of the fracture work by

$$\Delta G_{k,k+1} = h v_{N,k+\theta}^\top \sigma_c S \beta_{k+\theta} \approx \int_{t_k}^{t_{k+1}} v_N^\top \sigma_c S \beta \, dt. \quad (95)$$

We have the following estimate for the variation of the total mechanical energy for  $\frac{1}{2} < \theta \leq 1$ :

$$\Delta(K + U) + \Delta G_{k,k+1} - W_{\text{ext},k+1} < W_{\text{impact},k+1}. \quad (96)$$

Furthermore, it can be shown (see Acary (2016) for details) that the discretisation of the Moreau impact law (52) yields

$$W_{\text{impact},k+1} \leq 0 \text{ if } \theta \leq \frac{1}{1+e}, \quad (97)$$

and then, we obtain

$$\Delta(K + U) + \Delta G_{k,k+1} - W_{\text{ext},k+1} < W_{\text{impact},k+1} \leq 0. \quad (98)$$

For  $\theta = \frac{1}{2}$ , and then for any value of  $e \in [0, 1]$ , the incremental energy balance can be refined to

$$\Delta(K + U) + \Delta G_{k,k+1} - W_{\text{ext},k+1} = W_{\text{impact},k+1} \leq 0. \quad (99)$$

Comparing to the energy balance (39), we conclude that the incremental discrete energy balance, provided by the time-stepping scheme, ensures the practical stability of the scheme by not spuriously adding energy into the system.

## 5 Numerical validations

We implement our discretised system in Python, and we solve the LCP using the Siconos software (Acary et al., 2019), and use the robust Lemke (Lemke and Howson, Jr., 1964) algorithm to resolve the system. While other (possibly faster) algorithm choices are available, Lemke guarantees that the correct solution to the LCP will be found, within numerical precision.

### 5.1 Quasi-static scalar case with elastic spring

For the sake of illustration, we will consider firstly a static system. Let us consider the case of an elastic rod bound onto a rigid substrate with a cohesive zone, as outlined in Acary and Monerie (2006) and Chaboche et al. (2001), and depicted in Figure 3:

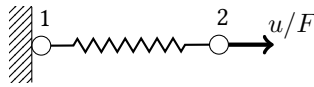


Figure 3: Two nodes joined by a spring. Node 1 features a cohesive zone bound onto a rigid substrate, while the driving displacement or force is applied to node 2.

First, we consider the structural stiffness matrix:

$$K = \begin{bmatrix} ES/\ell & -ES/\ell \\ -ES/\ell & ES/\ell \end{bmatrix}, \quad (100)$$

where  $\ell$  is the rod length,  $S$  the rod cross-sectional area (and area of the cohesive zone) and  $E$  is the Young's modulus of the rod. However, it is clear that this matrix is singular, so we modify it (and the external force  $F$ ) in order to enforce the boundary conditions and create an invertible matrix  $\bar{K}$ . If we consider (48) in static equilibrium (*i.e.* where we remove the  $Mv$  term from the equilibrium equation), we can conduct some simple re-arrangements to obtain an LCP for the general case of multiple cohesive zones,  $0 \leq w = Lz + q \perp z \geq 0$ . The discretisation otherwise follows (61), other than there being no  $\theta$ -method used,

as the velocities do not enter into the formulation. Thus, we have a fully implicit discretisation, giving the LCP

$$w = \begin{bmatrix} \beta_{k+1} \\ A^r_{k+1} \\ u_{N,k+1} \end{bmatrix}, \quad L = \begin{bmatrix} \mathbf{0} & -I & \mathbf{0} \\ I & \sigma_c \delta_c I - \sigma_c^2 H \bar{K}^{-1} H^\top S & -\sigma_c H \bar{K}^{-1} H^\top S \\ \mathbf{0} & \sigma_c H \bar{K}^{-1} H^\top S & H \bar{K}^{-1} H^\top S \end{bmatrix}, \quad z = \begin{bmatrix} \mu_{k+1} \\ h \lambda_{k+1} \\ \nu_{k+1} \end{bmatrix}, \quad (101)$$

$$q = \begin{bmatrix} \beta_k \\ -\sigma_c \left( \delta_c (\beta_k - 1) + H \bar{K}^{-1} (\bar{F}_{k+1} - \sigma_c H^\top S \beta_k) + b_{k+1} \right) \\ H \bar{K}^{-1} (\bar{F}_{k+1} - \sigma_c H^\top S \beta_k) + b_{k+1} \end{bmatrix}. \quad (102)$$

We can then solve this system for the case where the far end of the rod is driven according to the relation

$$u_2(t) = \begin{cases} \frac{1}{2}t & \text{for } 0 \leq t < 1, \\ 1 - \frac{1}{2}t & \text{for } 1 \leq t < 3, \\ -2 + \frac{1}{2}t & \text{for } 3 \leq t, \end{cases} \quad (103)$$

where extension is taken to be positive, and compression negative. The solution of the system (101) under driving input (103) with  $H = \begin{bmatrix} 1 & 0 \end{bmatrix}$ , material parameters  $\sigma_c = 0.5$  MPa,  $\delta_c = 1.0$  mm,  $E = 5.0$  MPa and  $\ell = 1.0$  mm, simulated for 8 ms with 4000 time steps is given in Figure 4:

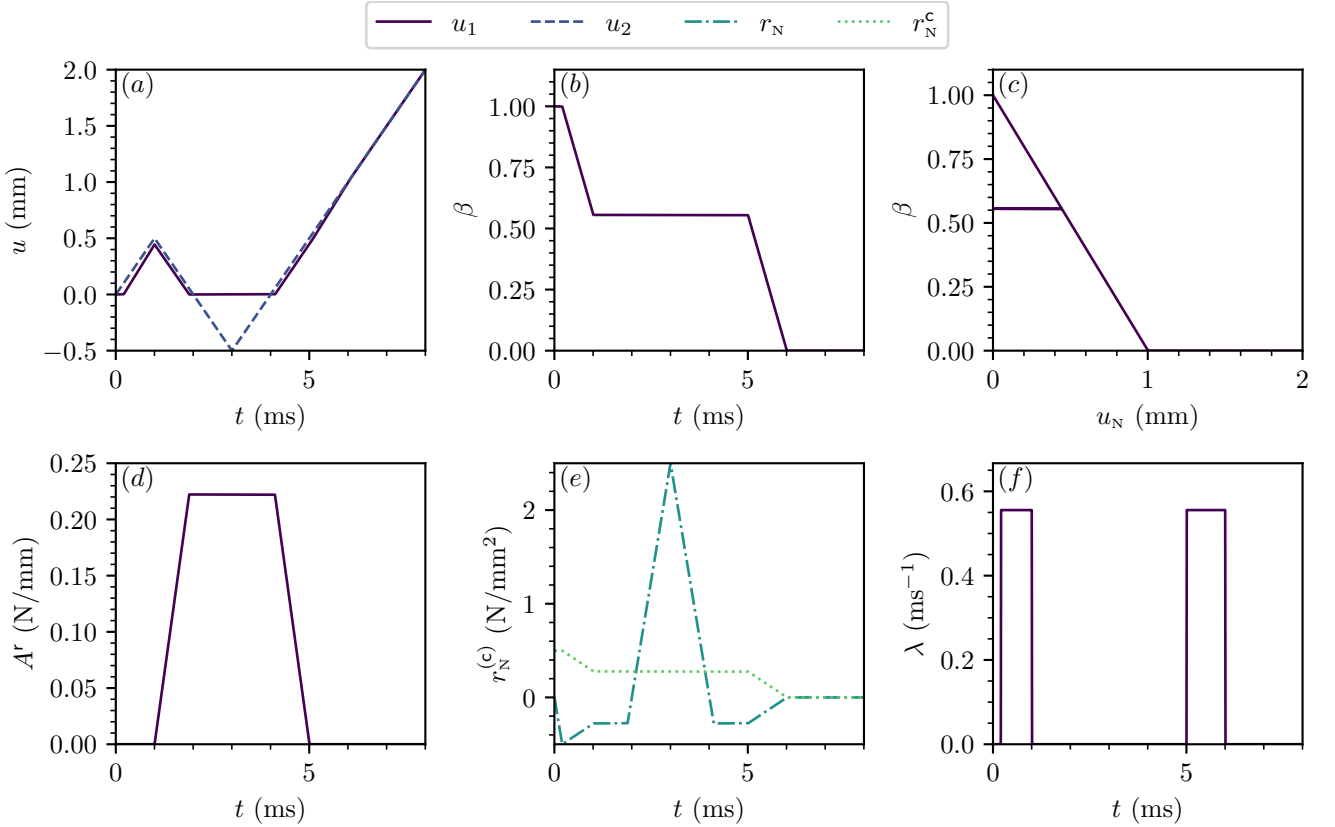


Figure 4: The solutions of the elastic bar with cohesive zone system. (a) The nodal displacements  $u_1$  and  $u_2$  as a function of time  $t$ . (b) The cohesion  $\beta$  as a function of time  $t$ . (c) The cohesion  $\beta$  as a function of crack opening displacement  $u_N$ . (d) The driving force  $A^r$  as a function of time  $t$ . (e) The reversible part of the reaction force  $r_N$  and the cohesive force  $r_N^c$  as a function of time  $t$ . (f) The rate of decohesion  $\lambda$  as a function of time  $t$ .

However, we must be careful that the behaviour of the system remains well-posed. When  $\sigma_c \delta_c I - H \bar{K}^{-1} H^\top S$  is no longer positive definite, the system loses uniqueness and multiple solutions are possible. So long as the condition

$$\sigma_c \delta_c \geq \frac{\ell}{E}, \quad (104)$$

is fulfilled, the system remains stable and there is a unique solution. Physically the unstable behaviour represents the accumulation of more elastic strain energy than can be released at the cohesive zone. Geometrically, the softening slope of the triangular

law is greater than the elastic stiffness of the system, resulting in both constitutive laws only being satisfied at  $u_N > \delta_c$  (see Chaboche et al. (2001) for further details). For the sake of illustration, we simulate the above system, but with  $E = 0.5$  in Figure 5:

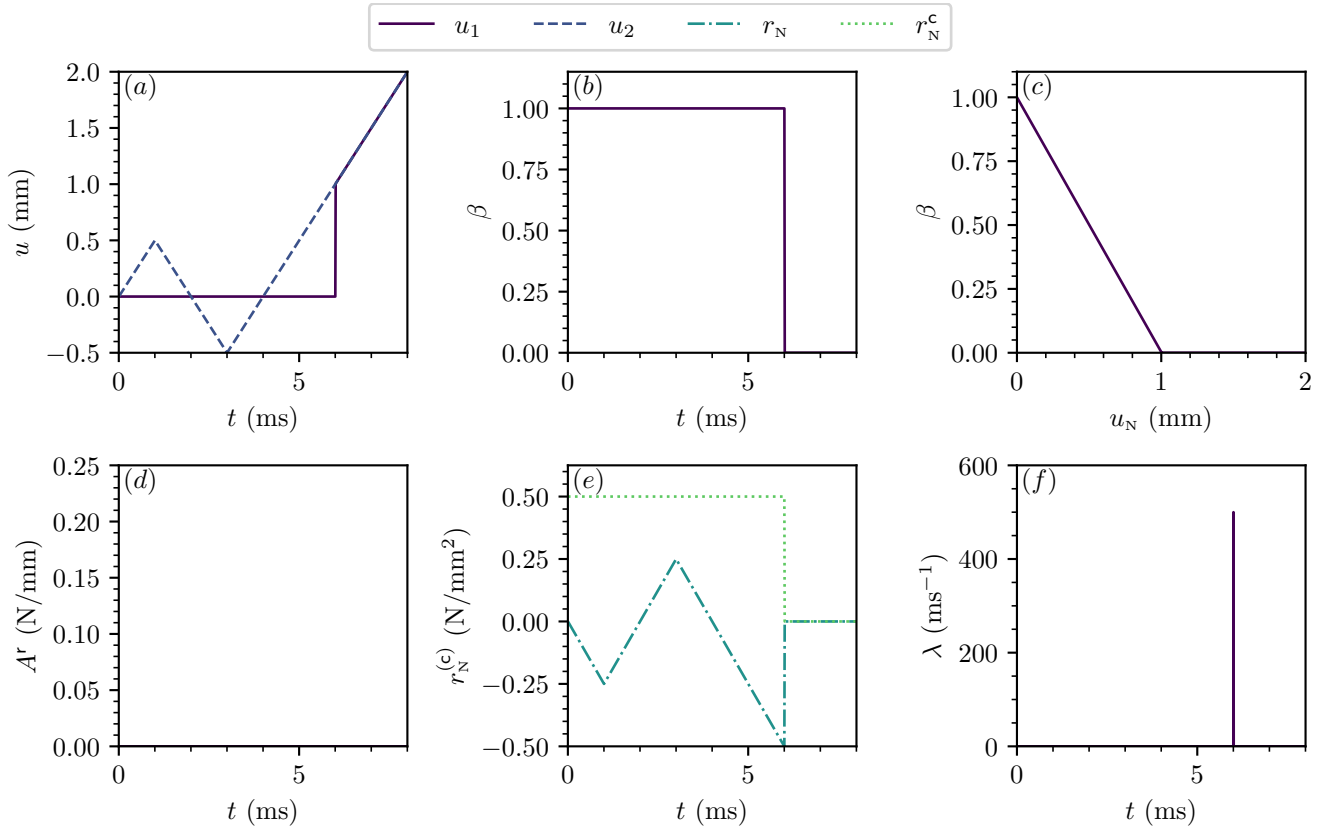


Figure 5: The solutions of the elastic bar with cohesive zone system for ill-posed system values. (a) The nodal displacements  $u_1$  and  $u_2$  as a function of time  $t$ . (b) The cohesion  $\beta$  as a function of time  $t$ . (c) The cohesion  $\beta$  as a function of crack opening displacement  $u_N$ . (d) The driving force  $A^r$  as a function of time  $t$ . (e) The reversible part of the reaction force  $r_N$  and the cohesive force  $r_N^c$  as a function of time  $t$ . (f) The rate of decohesion  $\lambda$  as a function of time  $t$ .

We may observe that the loss of uniqueness results in a “solution jump”, where the system moves from completely unbroken to completely broken in a single time step. More energy is stored elastically than can be released by the cohesive zone, resulting in the instantaneous rupture once the critical traction is achieved. It should also be noted that if larger time steps are chosen, the value of  $u_N$  at which  $\beta$  goes to zero is subject to “overshoot”, meaning that an additional spurious energy release occurs.

This ill-posed system behaviour can be entirely avoided by working in dynamics, so from this point onwards we do so. However, as Figure 4 demonstrates, the model can be successfully implemented in statics, provided that the condition given in (104) is always respected.

## 5.2 Dynamic cohesive zone model with elasticity

### 5.2.1 Dynamic case with single elastic spring

Now, we consider the same system as above, but this time in dynamics. We use the system parameters  $\sigma_c = 0.5$  MPa,  $\delta_c = 1.0$  mm,  $e = 0.0$ ,  $E = 0.5$  MPa,  $l = 1$  mm,  $S = 1$  mm<sup>2</sup>, and  $M = \begin{bmatrix} 0.25 & 0 \\ 0 & 0.25 \end{bmatrix}$  g. These values result in an ill-posed system in the static case, but as we demonstrate below, the addition of dynamics regularises the system. We simulate the system for 8 ms using 4000 time steps and  $\theta = 1$ , subject to the same driving displacement (103). We observe the system evolution depicted in Figure 6:

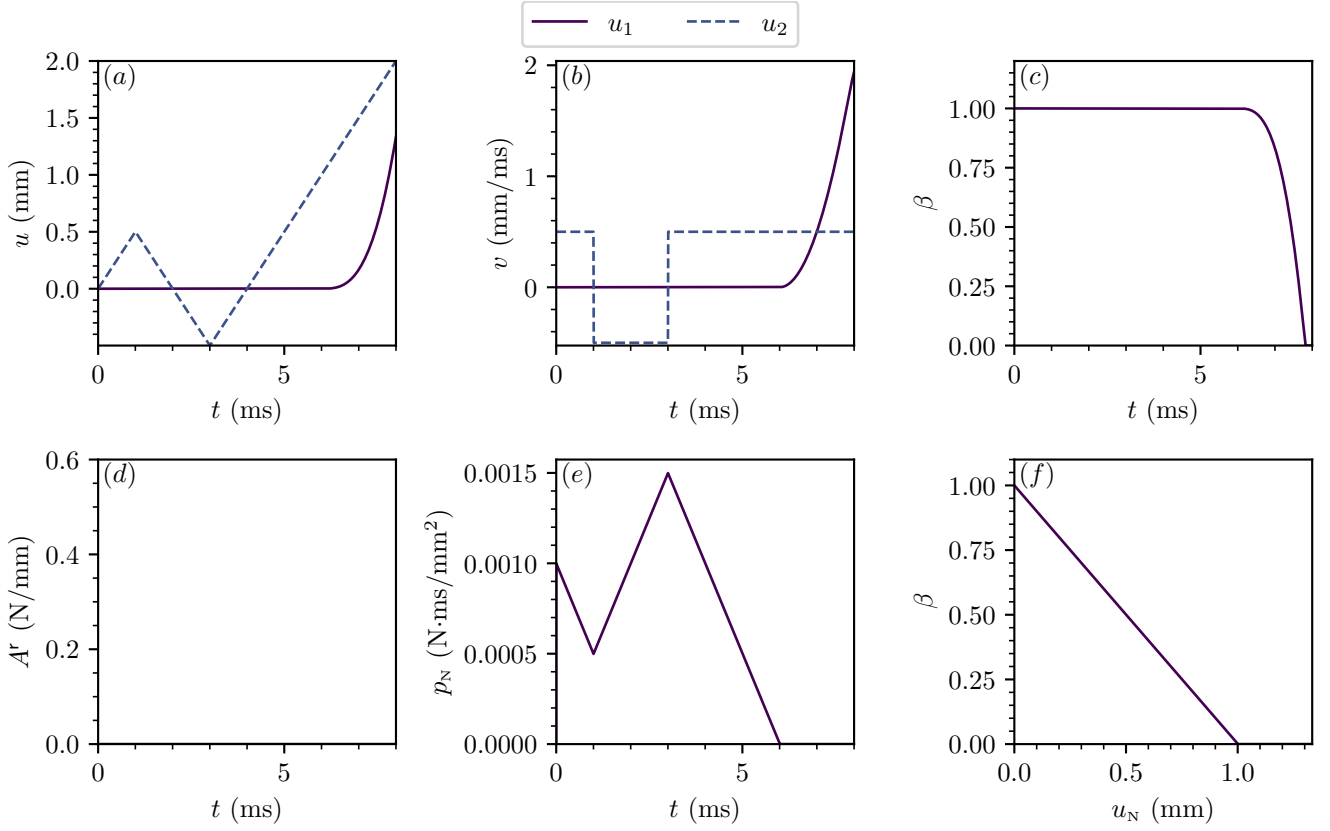


Figure 6: The solutions of the dynamic CZM system with elasticity, for values that are ill-posed in statics. (a) The displacements  $u$  as a function of time  $t$ . (b) The velocities  $v$  as a function of time  $t$ . (c) The cohesion  $\beta$  as a function of time  $t$ . (d) The thermodynamic driving force  $A^r$  as a function of time  $t$ . (e) The percussion  $p_N$  as a function of time  $t$ . (f) The cohesion  $\beta$  as a function of crack opening displacement  $u_N$ .

We may observe in Figure 6 that the inertial effects result in a smoothly changing value of  $\beta$  with time, as opposed to the instantaneous rupture of the equivalent system in statics, thus demonstrating the well-posed nature of the system.

In order to demonstrate the effect of including percussions in the formulation, we may simulate the same system of a spring attached to a cohesive zone, but with different parameters and subject to a different driving force. We use the system parameters  $\sigma_c = 1.0$  MPa,  $\delta_c = 1.0$  mm,  $e = 0.0$ ,  $E = 10$  MPa,  $l = 1$  mm,  $S = 1$  mm<sup>2</sup>, and  $M = \begin{bmatrix} 2.5 & 0 \\ 0 & 2.5 \end{bmatrix}$  g. The system is subject to the driving force in Newtons:

$$F = 1.5\sigma_c \exp(0.25t) \sin(\pi t). \quad (105)$$

We observe the system evolution depicted in Figure 7:

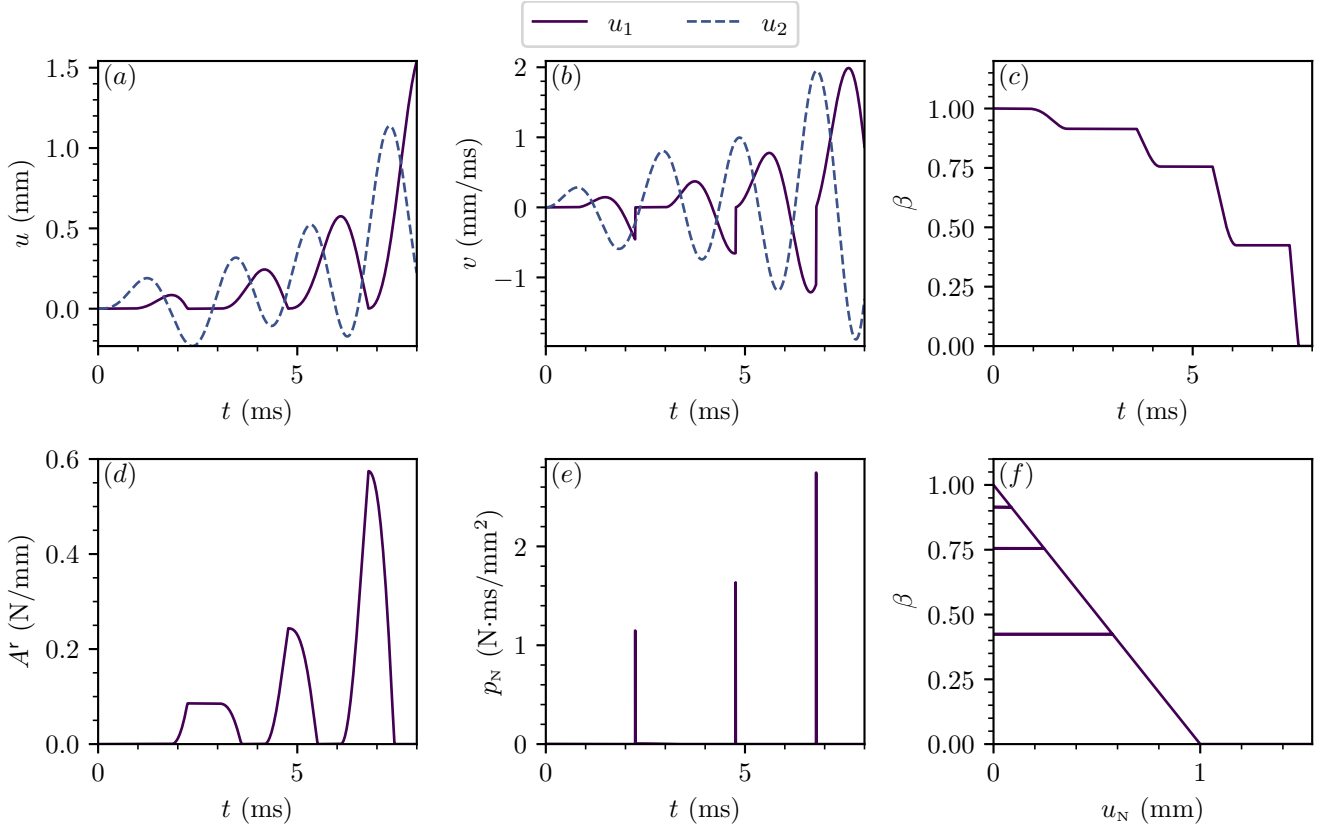


Figure 7: The solutions of the dynamic CZM system with elasticity. (a) The displacements  $u$  as a function of time  $t$ . (b) The velocities  $v$  as a function of time  $t$ . (c) The cohesion  $\beta$  as a function of time  $t$ . (d) The thermodynamic force  $A^r$  as a function of time  $t$ . (e) The percussion  $p_N$  as a function of time  $t$ . (f) The cohesion  $\beta$  as a function of crack opening displacement  $u_N$ .

### 5.2.2 Dynamic double cantilever beam

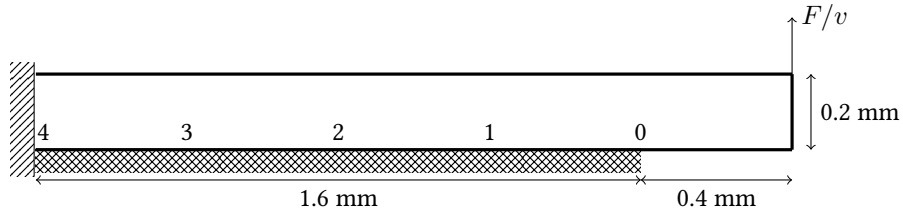


Figure 8: The symmetry of the double cantilever beam allows us to simulate it as a single cantilever beam fixed at the left end (diagonal hatching), with cohesive zone nodes attached to a rigid substrate along the symmetry plane (cross hatching). A force or velocity is applied at the upper right hand corner, at the free end. We follow the decohesion at the points labelled 0 through 4.

We simulate a double cantilever beam (DCB) shown in Figure 8 inspired by that found in Camacho and Ortiz (1996), but using parameters for polymethyl methacrylate (PMMA). We simulate a DCB with a length of 2 mm, with a pre-existing crack of 0.4 mm length. The beam is taken to have a thickness of 1 mm, and to be loaded in plane stress. The beam is meshed using Gmsh 4.8.1 (Geuzaine and Remacle, 2009), and read into Python with Meshio 5.3.0 (Schlömer, 2022) (as are all the finite element meshes in this work). The bulk material has Young's modulus  $E = 2.7 \times 10^3$  MPa, a Poisson's ratio  $\nu = 0.39$  (Doitrand et al., 2021b), and a mass density  $\rho = 1.18 \times 10^{-3}$  g/mm<sup>3</sup> (Doitrand et al., 2019). We use constant strain (T3) triangular elements in our finite element discretisation, with a consistent mass matrix. The cohesive zone parameters are the critical traction  $\sigma_c = 45$  MPa, the fracture energy  $G_c = 0.14$  N/mm, and the critical distance  $\delta_c = 0.0062$  mm, while the coefficient of restitution  $e = 0$ .

We simulate only half the system, exploiting the symmetry inherent to the problem. Thus, the lower boundary of the system consists of a series of nodes with cohesive zones attached, excepting a section representing an initial crack. It is important to note that where the Dirichlet boundary intersects with the cohesive zone boundary, the node is removed from the set of cohesive zone nodes, and its tributary area is allocated to the neighbouring cohesive node. Thus, the crack is allowed to propagate over the entire length of the system, but there is no possibility of the LCP being made infeasible by trying to enforce the Dirichlet boundary condition on a cohesive zone node. The mesh is shown in Figure 9:

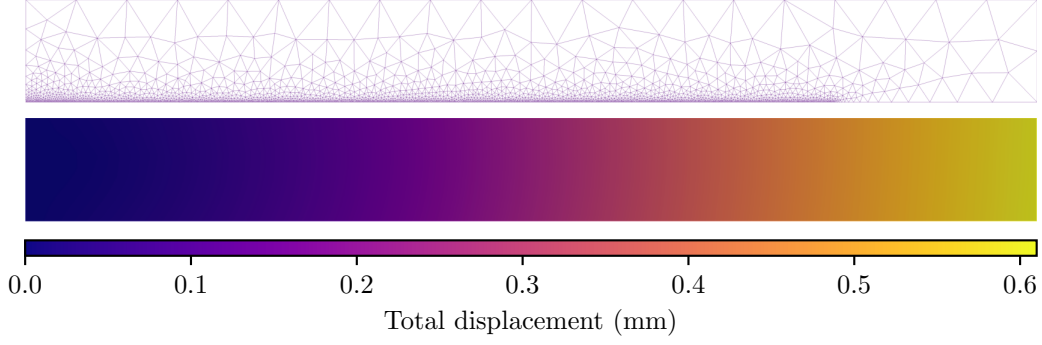


Figure 9: The mesh of the double cantilever beam, and the total displacements of the mesh at the end of the controlled displacement test, measured by the norm of the displacements at each node.

We simulate the upper half of the DCB using a controlled displacement test, displacing at the rate of 1 mm/ms to a target displacement at the free end of 0.6 mm. We set  $\theta = 0.5$ , and adopt a large initial time step of  $h = 0.0015$  ms, so that the loading stage before the crack initiates is not overly time-consuming. Once the crack initiates, we enforce a smaller time step of  $h = 2.5 \times 10^{-4}$  ms, ensuring that the LCP remains well-posed. In principle, we also allow adaptive time-stepping (dividing the time step in half) in the event that the LCP does not resolve correctly, however, this condition is never activated during the simulation. We insist on the fact that this time step is relatively large compared to simulations performed with intrinsic models which require small time steps due to the initial stiffness of the system. The results of the simulation are shown in Figure 10:

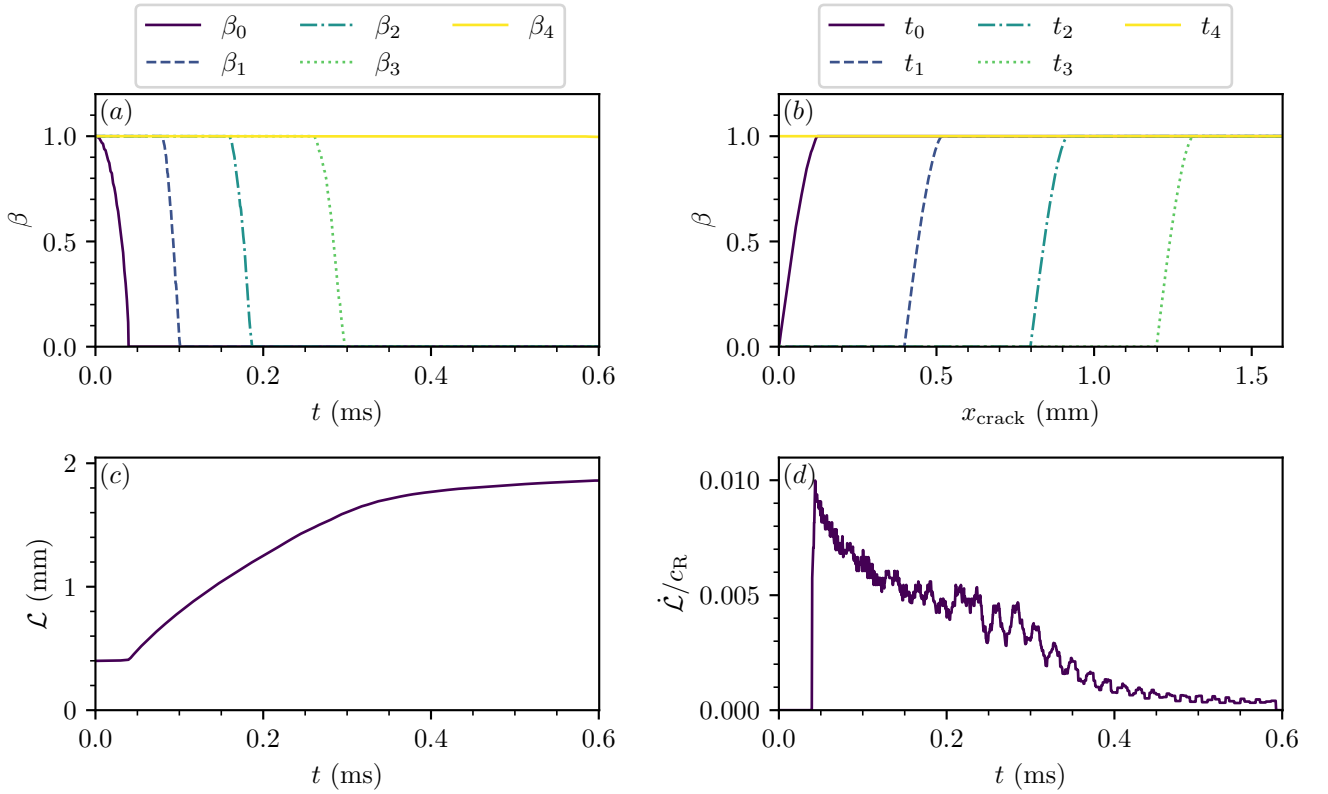


Figure 10: The simulation of a double cantilever beam under velocity control. (a) The cohesion  $\beta$  as a function of time  $t$  at the points of interest. (b) The cohesion  $\beta$  as a function of distance from the tip of the initial crack  $x_{\text{crack}}$ , at the times that the cohesion of each of the points of interest goes to zero. (c) The length  $\mathcal{L}$  of the crack as a function of time  $t$ . (d) The crack tip velocity  $\dot{\mathcal{L}}$  normalised by the Rayleigh wave speed  $c_R$ , as a function of time  $t$ .

The Rayleigh wave  $c_R$  speed is calculated by

$$c_R = \sqrt{\frac{E}{2\rho(1+\nu)} \frac{0.886 + 1.14\nu}{1+\nu}}, \quad (106)$$

which is a good approximation to the solution of the Rayleigh wave function (Freund, 1998). We apply a Savitzky-Golay filter (Savitzky and Golay, 1964) to the crack length in order to smooth the signal slightly. A window of 31 time steps and a first-order polynomial is observed to reduce the noise sufficiently so that the underlying velocity trend is legible. The crack tip velocity is then calculated by assuming a linear growth rate between the spatial points as they crack. We may observe in Figure 10 that the speed of the decohesion gradually declines over time, other than for the very first point to crack, which takes substantially longer than the others. Some slowing of the initial decohesion is observable in the curve for  $\beta_3$  in subfigure (a), as a result of the influence of the geometry of the problem. In subfigure (b), we can see that the size of the fracture process zone remains essentially constant throughout the cracking process. Subfigures (c) and (d) demonstrate the relatively steady growth in the crack length, with an initial sharp increase occurring as the crack establishes before gradually tapering away. We also note that the crack velocity is very small relative to the mode I theoretical limit of  $c_R$ , due to both geometrical effects and the low velocity at which the displacement is controlled.

We can also consider the energy-conserving properties of the integration scheme, by plotting the changing energetic quantities:

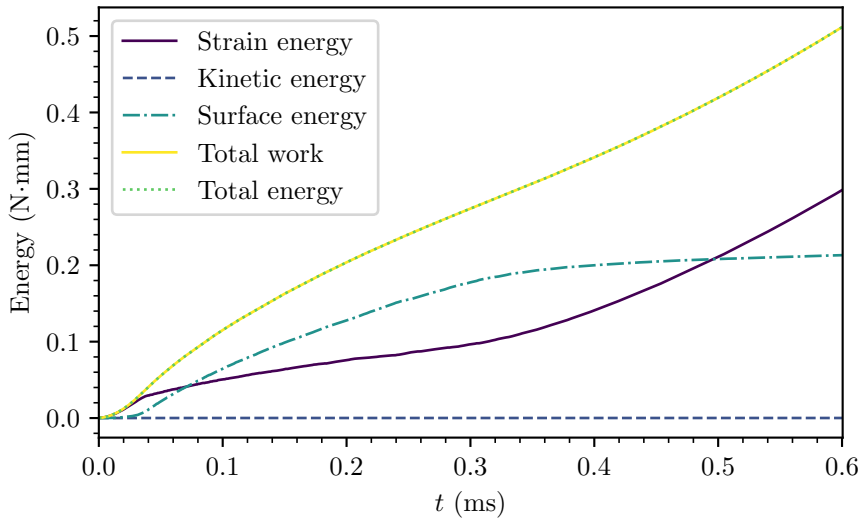


Figure 11: The energies of the dynamic double cantilever beam simulation under velocity control.

We can see in Figure 11, that the work input matches exactly with the sum of the strain, kinetic and expended cohesive energies, indicating that the integration scheme successfully conserves the energy. As the crack grows, a comparatively greater share of the work input is used in the creation of new surface area than in the storage of strain energy, while the kinetic energy remains negligible (as is to be expected in a slow displacement-controlled simulation). However, at the point at which the crack is constrained from further growth, elastic energy becomes the dominant fraction of the total energy.

We also simulate the same system under force control, this time increasing the loading (in Newtons) according to  $F = 10t$  until one element is fully decohered, at which point the force is held constant. The results of the simulation are shown in Figure 12:

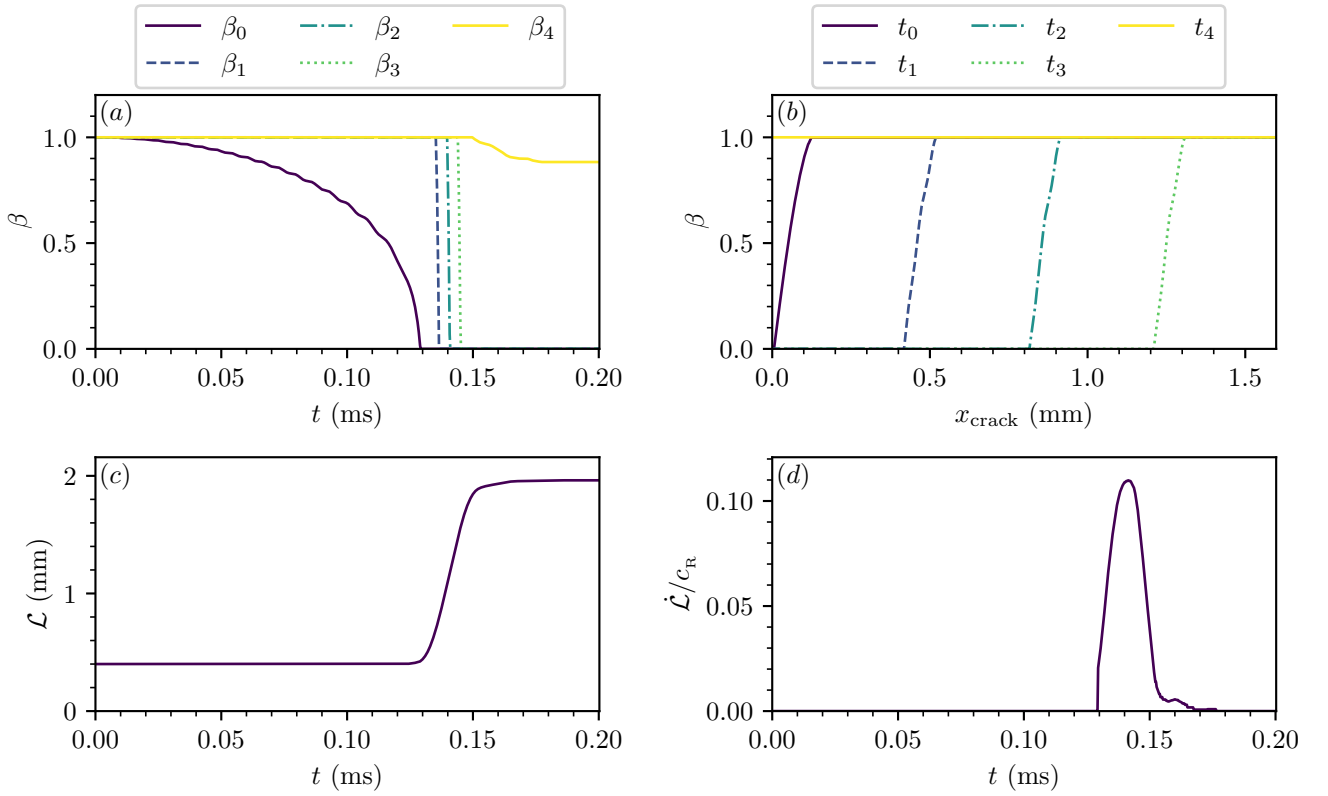


Figure 12: The simulation of a double cantilever beam under force control. (a) The cohesion  $\beta$  as a function of time  $t$  at the points of interest. (b) The cohesion  $\beta$  as a function of distance from the tip of the initial crack  $x_{\text{crack}}$ , at the time that the cohesion of each of the points of interest goes to zero. (c) The length  $\mathcal{L}$  of the crack as a function of time  $t$ . (d) The crack tip velocity  $\dot{\mathcal{L}}$  normalised by the Rayleigh wave speed  $c_R$ , as a function of time  $t$ .

Once again, we apply a Savitzky-Golay filter with a window size of 31 time steps and a first order polynomial on the crack length  $L$ , to reduce the noise when calculating  $\dot{\mathcal{L}}$ . In comparing Figure 10 and Figure 12, we may observe that the force-controlled system decoheres much more slowly initially, up until the point at which the crack begins, where it then travels much more rapidly than the velocity-controlled system, with crack arrest being achieved by the interaction with the fixed boundary of the system. This geometry, as well as the small applied force, once again results in the crack being slow in comparison with the theoretical limit of  $c_R$ , although at the peak velocity it is approximately an order of magnitude faster than the speed of the crack under velocity control. We note that the decohesion of points 1, 2 and 3 are more rapid and more concentrated in time than for the velocity controlled system, and that point 4 experiences some decohesion, whereas it remained intact for the velocity controlled system. Once again, we can also consider the energetic properties of the system:

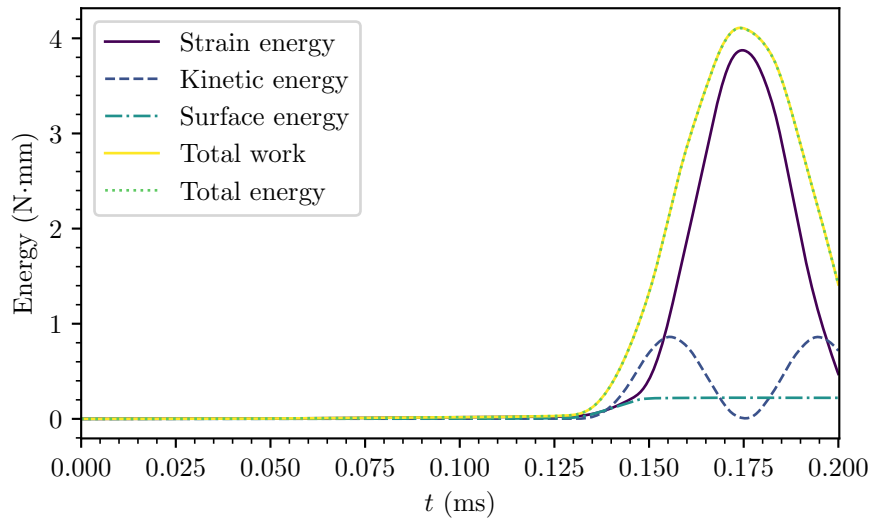


Figure 13: The energies of the dynamic double cantilever beam simulation under force control.

We may observe that the energetic behaviour of this system depicted in Figure 13 is rather different to that of the velocity controlled system. We observe that the system is truly dynamic, and a significant part of the work input is transformed into kinetic energy. We also observe that at a certain point, the work input decreases and the system moves towards its equilibrium state, with a certain amount of surface energy, and exchanges between the strain and kinetic energies. We note that total system energy matches exactly the total work input, indicating that the numerical schema successfully conserves energy in a simulation with more dynamic effects.

### 5.2.3 Rhombus hole specimen

As a more direct comparison of our method against an equivalent intrinsic model, we also simulate the rhombus hole specimen in Doitrand et al. (2019), applying (69) with the same principles as for the DCB. The sample has a width of 40 mm and a height of 60 mm, with a rhombus hole in the centre that has a corner angle  $\gamma$  and a half-diagonal length of 4.95 mm. The sample has a thickness of 10 mm, and is simulated in plane strain (Doitrand, personal communication).

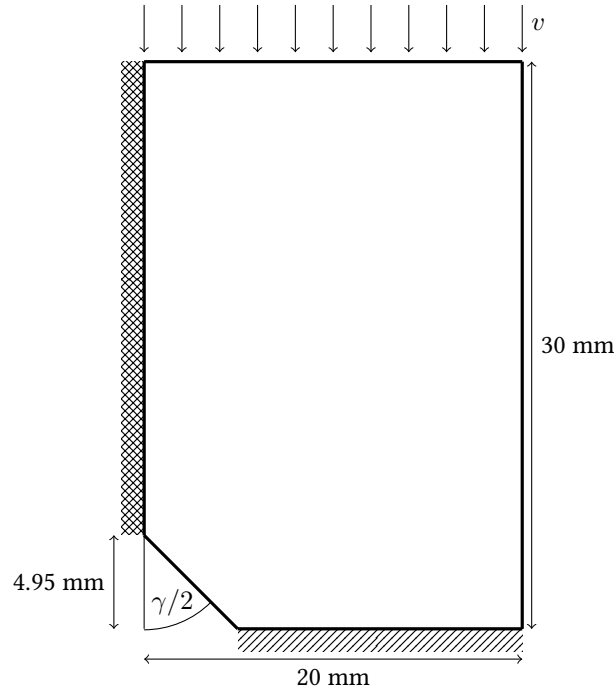


Figure 14: The double symmetry of the rhombus hole specimen allows us to simulate only the top right quarter. Standard symmetry conditions (diagonal hatching) are applied to the bottom boundary, while cohesive zone nodes and a symmetry condition are attached to the left boundary (cross hatching). A velocity is applied uniformly to all points on the top boundary. The vertical half diagonal retains a constant length, but the angle  $\gamma$  is varied to produce different geometries.

We exploit symmetry so that we need only simulate one quarter (the top-right) of the sample. The boundary conditions on the left and bottom edges are thus symmetry conditions, with normal displacements restricted to be positive or zero, and tangential displacements unrestrained. The right edge and the rhombus hole edge are similarly unrestrained, while the loading is applied as a Dirichlet condition on the top edge. As the crack is predicted to occur along the left edge, these nodes are included in the set of cohesive zone nodes. The 1 mm length closest to the corner of the rhombus hole is allocated a very fine mesh, with one node every 0.002 mm, ensuring accurate resolution of the cohesive zone. The mesh is steadily coarsened to reach a characteristic size of 0.5 mm at the top of the left hand edge, while all of the bulk regions that exhibit purely elastic behaviour are allocated a characteristic size of 2 mm. Hence, the mesh is highly refined in the region of the crack process, while remaining computationally efficient. In order to better match the simulations of Doitrand et al. (2019), we use a quadrangular mesh, generated by the Blossom-Quad algorithm included in Gmsh (Remacle et al., 2012). The mesh is shown in Figure 15:

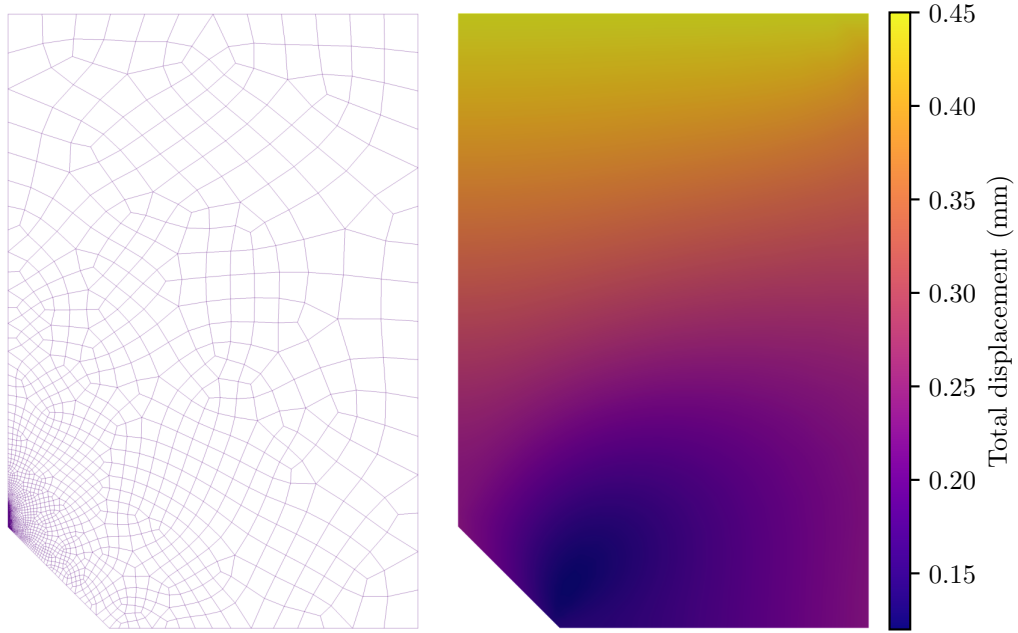


Figure 15: The mesh of the rhombus hole specimen for the angle  $\gamma = 90^\circ$ , and the total displacements of the mesh at the end of the test, measured by the norm of the displacements at each node.

The loading protocol is to impose a vertical displacement of a rate of 1 mm/s on the top edge, while also enforcing a no-slip condition, so that the horizontal velocities on the top edge are zero. At the time the first node cracks (*i.e.*  $\beta \leq 1 \times 10^{-12}$ ), the vertical loading is stopped and the displacement is held constant. The simulation continues until 20 time steps have passed with no changes in the value of  $\beta$  in any of the cohesive zone nodes.

The simulation is carried out with the values in Doitrand et al. (2019) representing PMMA, namely a Young's modulus  $E = 1600$  MPa, a Poisson's ratio  $\nu = 0.37$ , a density  $\rho = 1.19 \times 10^{-3}$  g/mm<sup>3</sup>, a critical traction  $\sigma_c = 80$  MPa, a fracture energy  $G_c = 0.25$  N/mm, and a coefficient of restitution  $e = 0$ . We use linear quadrangular (Q4) finite elements with full integration and a consistent mass matrix. We set  $\theta = 0.5$ , and our initial time step size as  $h = 4$  ms, up until the point that cracking occurs, when we set  $h = 1 \times 10^{-4}$  ms. We once again allow in-principle adaptive time-stepping if required to resolve the LCP, however the simulation successfully completes without activating this condition.

We can plot the results of the simulation in terms of the crack progression, once more tracking results at the points of interest, which in this case are the point at which the crack begins (index 0), the point at which the crack arrests (index 4), and the quarter, half and three-quarter points between them (indices 1, 2, and 3, respectively).

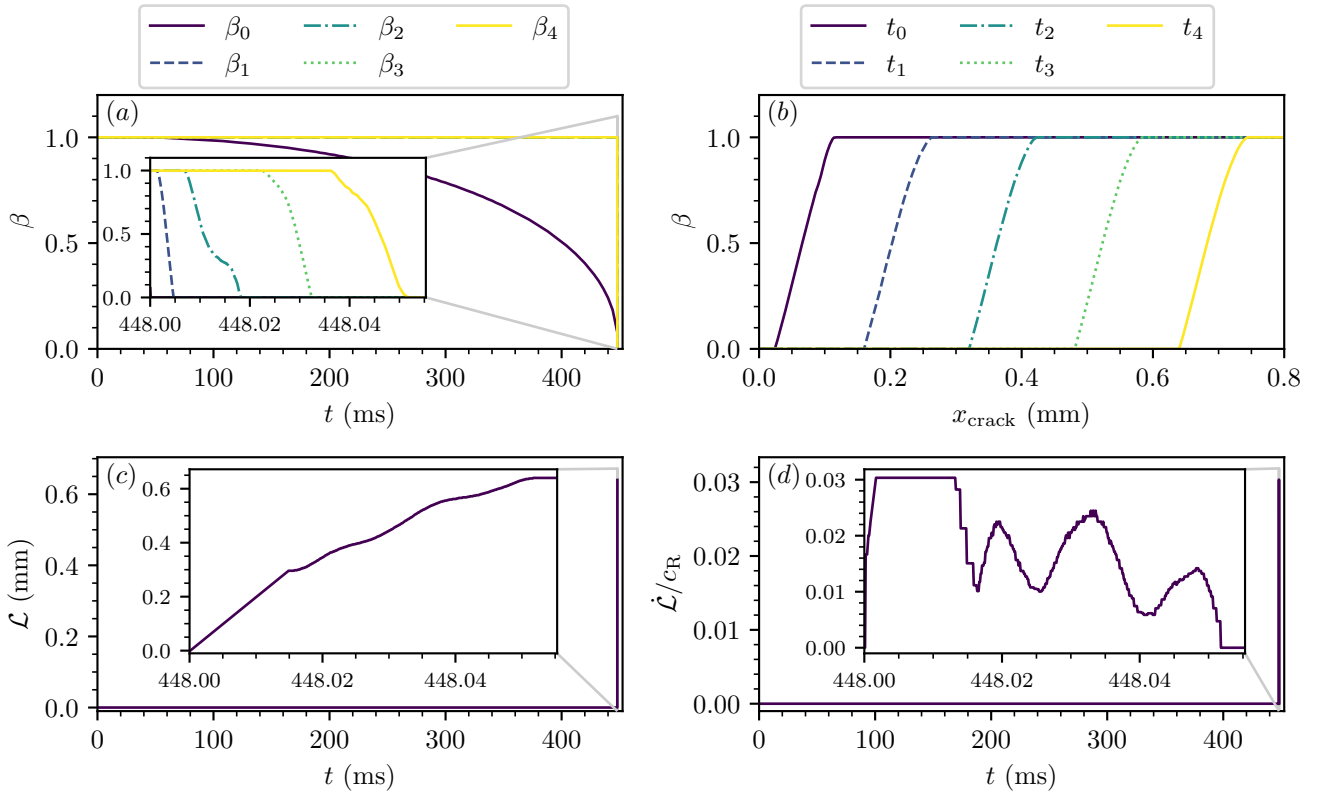


Figure 16: The simulation of a rhombus hole specimen with  $\gamma = 90^\circ$ . (a) The cohesion  $\beta$  as a function of time  $t$  at the quarter points. (b) The cohesion  $\beta$  as a function of distance from the tip of the initial crack  $x_{crack}$ , at the time that the cohesion of each of the quarter points goes to zero. (c) The length  $L$  of the crack as a function of time  $t$ . (d) The crack tip velocity  $\dot{L}$ , normalised by the Rayleigh wave speed  $c_R$ , as a function of time  $t$ .

Once again, we have applied a Savitzky-Golay filter of window size 31 time steps, and polynomial order 1 to the crack length, to obtain a smoother crack velocity. In this case, we observe several interesting behaviours in Figure 16. Unlike the relatively steady decohesion observed in the DCB, we observe that the node at the corner of the rhombus hole steadily decoheres over a long period of time, but once it reaches zero and the crack begins growing, the speed of decohesion is rapid (shown in the inset to (a)). Similarly, when considering the spatial distribution of the cohesion variable at the time each quarter point is fully decohered, we see that the length of the fracture process zone is essentially constant, as is the case with the DCB. The length of the crack grows with a velocity that appears to fluctuate around a decreasing overall trend. The final crack arrest length is 0.64 mm, which compares well with the value of 0.593 mm obtained by Doitrand et al. (2019).

Once again, we may also study the energetic properties of the solution algorithm that we implement:

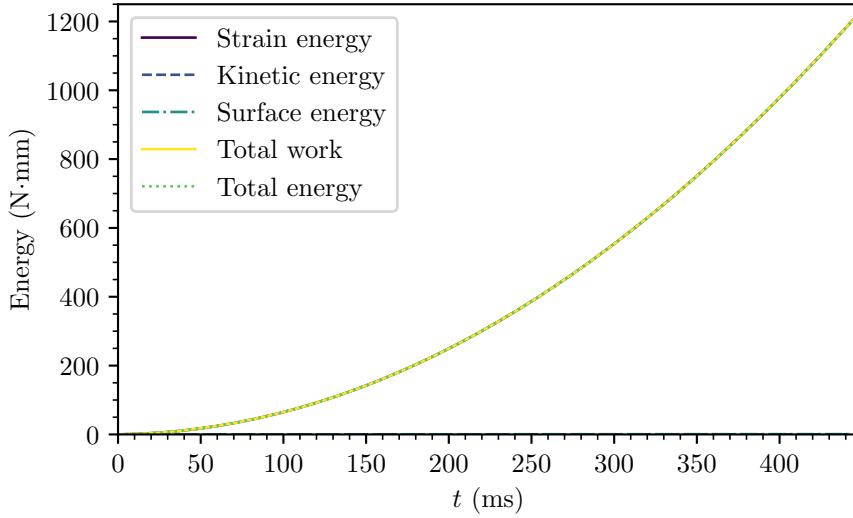


Figure 17: The energies of the rhombus hole simulation.

We can see that the strain energy accounts for the majority of the work input, while the kinetic energy and surface energy are both negligible.

As a final point of comparison, we may follow Doitrand et al. (2019), and vary the rhombus hole angle  $\gamma$  while observing the effect on the crack initiation force  $F_{\text{init}}$  and the crack arrest length  $\mathcal{L}_{\text{arrest}}$ . Some changes to the patterns of mesh refinement were made in the interests of computational efficiency, with a refined mesh being retained at the corner and in the region of the expected crack arrest point, but being less refined in between.

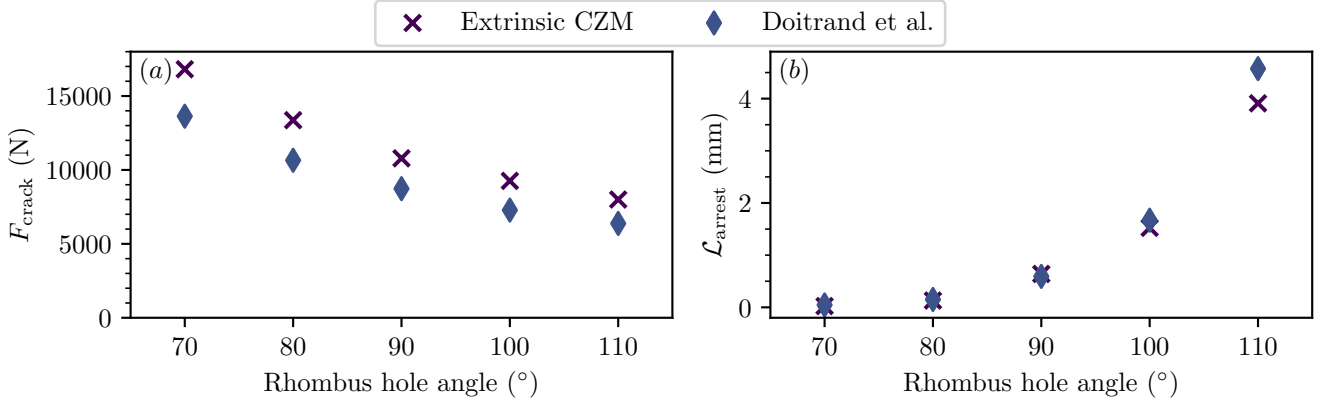


Figure 18: The results of simulations varying the rhombus hole angle  $\gamma$ . (a) The crack initiation force  $F_{\text{init}}$  at which cracking begins. (b) The crack arrest length  $\mathcal{L}$  at which crack propagation stops, in the absence of continued loading.

We may observe in Figure 18 that there is a good agreement between the results of the simulations in Doitrand et al. (2019), and the results of our models, with the initiation force decreasing and crack arrest length increasing as the rhombus hole angle increases. Possible reasons that may account for the differences may be the initial rigidity present in the CZM used by Doitrand et al. (2019) (they allocated an initial stiffness of  $1 \times 10^8$  MPa/mm), different meshes used to simulate the results, and different implementations of the cohesive zone between our finite elements and those of Abaqus. We note also that our results are achieved with substantially larger minimum time steps ( $1 \times 10^{-4}$  ms in our case, against  $1.5 \times 10^{-6}$  ms for Doitrand et al. (2019)). They also conducted a sensitivity analysis for the stiffness of the CZM using the  $90^\circ$  rhombus hole mesh, with the minimum time step size ranging from  $1 \times 10^{-4}$  ms for a stiffness of  $1 \times 10^6$  MPa/mm, down to  $2.4 \times 10^{-7}$  ms for a stiffness of  $1 \times 10^{10}$  MPa/mm. It is clear that our implementation of an extrinsic CZM is substantially more numerically efficient than a typical intrinsic CZM, in some cases by orders of magnitude.

## 6 Conclusions

In this paper, we first used the principle of virtual power to establish the equilibrium and boundary conditions of a body with a cohesive zone. Then, we postulated a free energy potential for the surface that allowed us to obtain non-smooth state laws of

the system. These state laws describe extrinsic cohesive zone models that do not have the “shifted intrinsic model” structure, thus guaranteeing appropriate physical behaviour under complex dynamic loading. By appropriately specifying a dissipative pseudo-potential, we obtained a complete generalised constitutive model of the cohesive zone system for normal crack opening, and demonstrated that while in this model decohesion is an irreversible process, it is also non-dissipative. We then specified a particular energetic potential in order to obtain a linear evolution of the cohesion variable with the displacement jump across the crack.

By appropriately discretising our system, and working with differential measures, we were able to include non-smooth impact dynamics within our model. The discretised system was combined with a  $\theta$ -method to obtain a time-stepping scheme that could be formulated as a linear complementarity problem. We then proved that the problem was well-posed for a sufficiently small time step, meaning that a solution exists, and that it is unique for certain variables. Moreover, it has been shown that the scheme has very good properties of conservation of energy balances.

We then implemented the model numerically by solving the complementarity problem at each time step. We demonstrated the system in statics, firstly parameter values leading to a well-posed problem, and then with values leading to an ill-posed problem. We then demonstrated that the same system in dynamics remains well-posed. Finally, we simulated some physical systems of interest by combining the linear complementarity problem with the finite element method. Both a double cantilever beam, and a rhombus hole sample were satisfactorily resolved, with the numerical scheme demonstrating good integration properties. The results of the rhombus hole simulations compared well with those of other authors in the literature, and were achieved with much larger time steps.

This work has demonstrated that applications of convex analysis can lead to physically correct and numerically efficient models for crack propagation. In this work, we decided to remain in a frictionless linear setting and to consider only a normal decohesion process to avoid excessive complexity in the presentation, but natural extensions of this work are to generalise the model to tangential displacements, adopt other possible forms of the cohesion evolution law, and to combine crack propagation with other physical phenomena.

**Acknowledgements** The authors thank Aurelian Doitrand, Rafael Estevez and Dominique Leguillon for kindly providing their data and Yann Monerie for fruitful discussions on the extrinsic cohesive model.

This work was carried out as part of Project SMART-PROTECT, financed by the Auvergne-Rhône-Alpes region.

**Code and Data availability** The code required to run the simulations described in this paper is available in a GitHub repository archived on [Software Heritage](#), or alternatively on [Zenodo](#). The data outputs of the codes are also available on [Zenodo](#).

## References

- Acary, V. and B. Brogliato (2008). *Numerical methods for nonsmooth dynamical systems. Applications in mechanics and electronics*. English. Lecture Notes in Applied and Computational Mechanics 35. Berlin: Springer. xxi, 525 p.
- Acary, V. and Y. Monerie (2006). *Nonsmooth fracture dynamics using a cohesive zone approach*. Anglais. Research Report RR-6032. INRIA, p. 56. URL: <http://hal.inria.fr/inria-00110560/en/>.
- Acary, V. et al. (2019). *An introduction to Siconos*. Tech. rep. Grenoble: INRIA.
- Acary, Vincent (May 2016). “Energy conservation and dissipation properties of time-integration methods for nonsmooth elastodynamics with contact”. In: *Journal of Applied Mathematics and Mechanics / Zeitschrift für Angewandte Mathematik und Mechanik* 96.5, pp. 585–603. DOI: [10.1002/zamm.201400231](https://doi.org/10.1002/zamm.201400231). URL: <https://hal.inria.fr/hal-01235240>.
- Ashouri Vajari, D., B.N. Legarth, and C.F. Niordson (Nov. 2013). “Micromechanical modeling of unidirectional composites with uneven interfacial strengths”. In: *European Journal of Mechanics, A/Solids* 42, pp. 241–250. ISSN: 09977538. DOI: [10.1016/j.euromechsol.2013.06.008](https://doi.org/10.1016/j.euromechsol.2013.06.008).
- Azab, M., G. Parry, and R. Estevez (Mar. 2020). “An analytical model for DCB/wedge tests based on Timoshenko beam kinematics for accurate determination of cohesive zone lengths”. In: *International Journal of Fracture* 222.1-2, pp. 137–153. ISSN: 15732673. DOI: [10.1007/s10704-020-00438-2](https://doi.org/10.1007/s10704-020-00438-2). URL: <https://doi.org/10.1007/s10704-020-00438-2>.
- Bergfeld, B. et al. (Dec. 2021). “Crack propagation speeds in weak snowpack layers”. In: *Journal of Glaciology*, pp. 1–14. ISSN: 0022-1430. DOI: [10.1017/JOG.2021.118](https://doi.org/10.1017/JOG.2021.118). URL: <https://www.cambridge.org/core/journals/journal-of-glaciology/article/crack-propagation-speeds-in-weak-snowpack-layers/C28905FA3198DF87B0A18AB135FC4766>.
- Berman, N., G. Cohen, and J. Fineberg (2020). “Dynamics and properties of the cohesive zone in rapid fracture and friction”. In: *Physical Review Letters* 125.12, p. 125503. ISSN: 10797114. DOI: [10.1103/PhysRevLett.125.125503](https://doi.org/10.1103/PhysRevLett.125.125503). URL: <https://doi.org/10.1103/PhysRevLett.125.125503>.
- Bourdin, B., G.A. Francfort, and J.-J. Marigo (2008). “The variational approach to fracture”. In: *Journal of elasticity* 91.1, pp. 5–148.
- Bybordiani, M. and D. Dias-da-Costa (Apr. 2021). “A consistent finite element approach for dynamic crack propagation with explicit time integration”. In: *Computer Methods in Applied Mechanics and Engineering* 376, p. 113652. ISSN: 00457825. DOI: [10.1016/j.cma.2020.113652](https://doi.org/10.1016/j.cma.2020.113652). URL: <https://doi.org/10.1016/j.cma.2020.113652%20https://linkinghub.elsevier.com/retrieve/pii/S0045782520308379>.
- Camacho, G.T. and M. Ortiz (1996). “Computational modelling of impact damage in brittle materials”. In: *International Journal of Solids and Structures* 33.20, pp. 2899–2938. ISSN: 0020-7683. DOI: [https://doi.org/10.1016/0020-7683\(95\)00255-3](https://doi.org/10.1016/0020-7683(95)00255-3). URL: <http://www.sciencedirect.com/science/article/pii/0020768395002553>.
- Carter, B. et al. (2000). “Parallel FEM simulation of crack propagation-challenges, status, and perspectives”. In: *Lecture Notes in Computer Science (including subseries Lecture Notes in Artificial Intelligence and Lecture Notes in Bioinformatics)*. Vol. 1800 LNCS. Springer Verlag, pp. 443–449. ISBN: 354067442X. DOI: [10.1007/3-540-45591-4\\_59](https://doi.org/10.1007/3-540-45591-4_59).
- Cazes, Fabien, Michel Coret, and Alain Combescure (2013). “A two-field modified lagrangian formulation for robust simulations of extrinsic cohesive zone models”. In: *Computational Mechanics* 51, pp. 865–884. URL: <https://hal.archives-ouvertes.fr/hal-00938515>.
- Célerié, F. et al. (2003). “Glass Breaks like Metal, but at the Nanometer Scale”. In: *Physical Review Letters* 90.7, p. 4. ISSN: 10797114. DOI: [10.1103/PhysRevLett.90.075504](https://doi.org/10.1103/PhysRevLett.90.075504).
- Chaboche, J.L., F. Feyel, and Y. Monerie (2001). “Interface debonding models: A viscous regularization with a limited rate dependency”. In: *International Journal of Solids and Structures* 38.18, pp. 3127–3160. ISSN: 00207683. DOI: [10.1016/S0020-7683\(00\)00053-6](https://doi.org/10.1016/S0020-7683(00)00053-6).
- Charlotte, M., J. Laverne, and J.-J. Marigo (2006). “Initiation of cracks with cohesive force models: a variational approach”. In: *European Journal of Mechanics-A/Solids* 25.4, pp. 649–669.
- Corre, T. et al. (June 2021). “Non steady-state intersonic cracks in elastomer membranes under large static strain”. In: *Journal of Theoretical, Computational and Applied Mechanics*. DOI: [10.46298/jtcam.6906](https://doi.org/10.46298/jtcam.6906). URL: <https://hal.archives-ouvertes.fr/hal-03006177v3%20https://jtcam.episciences.org/6906>.
- Cottle, R.W., J.-S. Pang, and R.E. Stone (2009). *The Linear Complementarity Problem*. Ed. by Robert E. O’Malley. Second. Philadelphia: Society for Industrial and Applied Mathematics, p. 781. ISBN: 978-0-89871-686-3. DOI: [10.1137/1.9780898719000](https://doi.org/10.1137/1.9780898719000). URL: <http://epubs.siam.org/doi/book/10.1137/1.9780898719000>.
- Crump, T. et al. (2017). “Dynamic fracture analysis by explicit solid dynamics and implicit crack propagation”. In: *International Journal of Solids and Structures* 110, pp. 113–126.
- Del Piero, G. (1999). “One-dimensional ductile-brittle transition, yielding, and structured deformations”. In: *IUTAM Symposium on Variations of Domain and Free-Boundary Problems in Solid Mechanics*. Springer, pp. 203–210.
- Doitrand, A., R. Estevez, and D. Leguillon (Feb. 2019). “Comparison between cohesive zone and coupled criterion modeling of crack initiation in rhombus hole specimens under quasi-static compression”. In: *Theoretical and Applied Fracture Mechanics* 99.November 2018, pp. 51–59. ISSN: 01678442. DOI: [10.1016/j.tafmec.2018.11.007](https://doi.org/10.1016/j.tafmec.2018.11.007). URL: <https://doi.org/10.1016/j.tafmec.2018.11.007%20https://linkinghub.elsevier.com/retrieve/pii/S0167844218304725>.

- Doitrand, A., R. Henry, and S. Meille (Mar. 2021a). “Brittle material strength and fracture toughness estimation from four-point bending test”. In: *Journal of Theoretical, Computational and Applied Mechanics*. DOI: [10.46298/jtcam.6753](https://doi.org/10.46298/jtcam.6753). URL: <https://jtcam.episciences.org/6753>.
- Doitrand, A. et al. (Jan. 2021b). “Experimental and theoretical characterization of mixed mode brittle failure from square holes”. In: *International Journal of Fracture*, pp. 1–11. ISSN: 15732673. DOI: [10.1007/s10704-020-00512-9](https://doi.org/10.1007/s10704-020-00512-9). URL: <https://doi.org/10.1007/s10704-020-00512-9>.
- Doyen, D., A. Ern, and S. Piperno (2010). “A three-field augmented Lagrangian formulation of unilateral contact problems with cohesive forces”. In: *ESAIM: Mathematical Modelling and Numerical Analysis* 44.2, pp. 323–346.
- (2013). “Quasi-explicit time-integration schemes for dynamic fracture with set-valued cohesive zone models”. In: *Computational Mechanics* 52.2, pp. 401–416.
- Espinha, R. et al. (2013). “Scalable parallel dynamic fracture simulation using an extrinsic cohesive zone model”. In: *Computer Methods in Applied Mechanics and Engineering* 266, pp. 144–161. ISSN: 0045-7825. DOI: <https://doi.org/10.1016/j.cma.2013.07.008>. URL: <http://www.sciencedirect.com/science/article/pii/S0045782513001783>.
- Falk, M.L., A. Needleman, and J.R. Rice (2001). “A critical evaluation of dynamic fracture simulations using cohesive surfaces”. In: *Journal de Physique IV, (in press) 2001*.
- Foulk, J.W. (Jan. 2010). “An examination of stability in cohesive zone modeling”. In: *Computer Methods in Applied Mechanics and Engineering* 199.9-12, pp. 465–470. ISSN: 0045-7825. DOI: [10.1016/J.CMA.2009.08.025](https://doi.org/10.1016/J.CMA.2009.08.025).
- Frémond, M. (1988). “Contact with Adhesion”. In: *Nonsmooth Mechanics and Applications*. Vienna: Springer Vienna, pp. 177–221. DOI: [10.1007/978-3-7091-2624-0\\_3](https://doi.org/10.1007/978-3-7091-2624-0_3). URL: [http://link.springer.com/10.1007/978-3-7091-2624-0\\_3](http://link.springer.com/10.1007/978-3-7091-2624-0_3).
- (2002). *Non-Smooth Thermomechanics*. Berlin, Heidelberg: Springer Berlin Heidelberg. ISBN: 978-3-642-08578-9. DOI: [10.1007/978-3-662-04800-9](https://doi.org/10.1007/978-3-662-04800-9). URL: <http://link.springer.com/10.1007/978-3-662-04800-9>.
- (2012a). “Contact with Adhesion”. In: *Phase Change in Mechanics*. Vol. 13. Lecture Notes of the Unione Matematica Italiana 4. Berlin, Heidelberg: Springer Berlin Heidelberg, pp. 151–156. ISBN: 978-3-642-24608-1. DOI: [10.1007/978-3-642-24609-8](https://doi.org/10.1007/978-3-642-24609-8). URL: <http://link.springer.com/10.1007/978-3-642-24609-8>.
- (2012b). “Damage of Solids Glued on One Another: Coupling of Volume and Surface Damages”. In: *Phase Change in Mechanics*. Lecture Notes of the Unione Matematica Italiana. Berlin, Heidelberg: Springer Berlin Heidelberg, pp. 115–130. ISBN: 978-3-642-24608-1. DOI: [10.1007/978-3-642-24609-8](https://doi.org/10.1007/978-3-642-24609-8). URL: <http://link.springer.com/10.1007/978-3-642-24609-8>.
- Freund, L.B. (1998). *Dynamic Fracture Mechanics*. Second. Cambridge: Cambridge University Press.
- Geuzaine, C. and J.-F. Remacle (Sept. 2009). “Gmsh: A 3-D finite element mesh generator with built-in pre- and post-processing facilities”. In: *International Journal for Numerical Methods in Engineering* 79.11, pp. 1309–1331. ISSN: 00295981. DOI: [10.1002/nme.2579](https://doi.org/10.1002/nme.2579). URL: <http://doi.wiley.com/10.1002/nme.2579>.
- Griffith, A.A. (Jan. 1921). “The phenomena of rupture and flow in solids”. In: *Philosophical Transactions of the Royal Society of London. Series A: Mathematical, Physical and Engineering Sciences* 221.582-593, pp. 163–198. ISSN: 0264-3952. DOI: [10.1098/rsta.1921.0006](https://doi.org/10.1098/rsta.1921.0006). URL: <https://royalsocietypublishing.org/doi/10.1098/rsta.1921.0006>.
- Guilloteau, E., H. Charrue, and F. Creuzet (1996). “The direct observation of the core region of a propagating fracture crack in glass”. In: *Europhysics Letters (EPL)* 34.7, pp. 549–554. ISSN: 0295-5075. DOI: [10.1209/epl/i1996-00493-3](https://doi.org/10.1209/epl/i1996-00493-3).
- Halphen, B. and Q.S. Nguyen (Jan. 1, 1975). “Sur les Matériaux Standard Généralisés”. In: *Journal de Mécanique* 14, pp. 39–63.
- Houlsby, G.T. (2019). “Frictional Plasticity in a Convex Analytical Setting”. In: *Open Geomechanics* 1.3, pp. 1–10. DOI: [10.5802/ogeo.2](https://doi.org/10.5802/ogeo.2). URL: [https://opengeomechanics.centre-mersenne.org/item/OGEO\\_2019\\_\\_1\\_A3\\_0](https://opengeomechanics.centre-mersenne.org/item/OGEO_2019__1_A3_0).
- Jean, M. (July 1999). “The non-smooth contact dynamics method”. In: *Computer Methods in Applied Mechanics and Engineering* 177.3-4, pp. 235–257. ISSN: 00457825. DOI: [10.1016/S0045-7825\(98\)00383-1](https://doi.org/10.1016/S0045-7825(98)00383-1). URL: <https://linkinghub.elsevier.com/retrieve/pii/S0045782598003831>.
- Jean, M., V. Acary, and Y. Monerie (2001). “Non Smooth Contact dynamics approach of cohesive materials”. In: *Philosophical Transactions : Mathematical, Physical & Engineering Sciences, The Royal Society, London A* A359.1789, pp. 2497–2518.
- Jean, M. and J.J. Moreau (1992). “Unilaterality and dry friction in the dynamics of rigid body collections”. In: *1st Contact Mechanics International Symposium*. Ed. by A. Curnier. Lausanne, pp. 31–48. URL: <https://hal.archives-ouvertes.fr/hal-01863710>.
- Jiang, S. et al. (Sept. 2021). “Characterisation of fracture evolution of a single cemented brittle grain using in-situ X-ray computed tomography”. In: *International Journal of Rock Mechanics and Mining Sciences* 145, p. 104835. ISSN: 1365-1609. DOI: [10.1016/J.IJRMMS.2021.104835](https://doi.org/10.1016/J.IJRMMS.2021.104835).
- Kubair, D.V. and P.H. Geubelle (2003). “Comparative analysis of extrinsic and intrinsic cohesive models of dynamic fracture”. In: *International Journal of Solids and Structures* 40.15, pp. 3853–3868. ISSN: 0020-7683. DOI: [https://doi.org/10.1016/S0020-7683\(03\)00171-9](https://doi.org/10.1016/S0020-7683(03)00171-9). URL: <http://www.sciencedirect.com/science/article/pii/S0020768303001719>.
- Laiarindrasana, L. et al. (Oct. 2021). “Ductile crack initiation and growth on a plasticized Polyvinylchloride during air bag deployment”. In: *Journal of Theoretical, Computational and Applied Mechanics*. DOI: [10.46298/jtcam.7401](https://doi.org/10.46298/jtcam.7401). URL: <https://hal.archives-ouvertes.fr/hal-03206110v2https://jtcam.episciences.org/7401>.

- Lemke, C.E. and J.T. Howson, Jr. (June 1964). "Equilibrium Points of Bimatrix Games". In: *Journal of the Society for Industrial and Applied Mathematics* 12.2, pp. 413–423. ISSN: 0368-4245. DOI: [10.1137/0112033](https://doi.org/10.1137/0112033). URL: <http://epubs.siam.org/doi/10.1137/0112033>.
- Lorentz, E. (2008). "A mixed interface finite element for cohesive zone models". In: *Computer Methods in Applied Mechanics and Engineering* 198.2, pp. 302–317. ISSN: 0045-7825. DOI: <https://doi.org/10.1016/j.cma.2008.08.006>. URL: <https://www.sciencedirect.com/science/article/pii/S0045782508002880>.
- Marazzato, F. (2020). "Discrete element and time-integration methods for elasto-plasticity and dynamic cracking". PhD thesis. Université Paris-Est Marne-la-Vallée (UPEM).
- Marigo, J.-J. (1981). "Formulation d'une loi d'endommagement d'un matériau élastique". In: *Comptes rendus de l'Académie des sciences. Série 2, Mécanique, Physique, Chimie, Sciences de l'univers, Sciences de la Terre* 292.May, pp. 1309–1312.
- Michel, J.C. and P. Suquet (May 1994). "An analytical and numerical study of the overall behaviour of metal-matrix composites". In: *Modelling and Simulation in Materials Science and Engineering* 2.3A, p. 637. ISSN: 0965-0393. DOI: [10.1088/0965-0393/2/3A/015](https://doi.org/10.1088/0965-0393/2/3A/015). URL: <https://iopscience.iop.org/article/10.1088/0965-0393/2/3A/015>. URL: <https://iopscience.iop.org/article/10.1088/0965-0393/2/3A/015/meta>.
- Monerie, Y. and V. Acary (2001). "Formulation dynamique d'un modèle de zone cohésive tridimensionnel couplant endommagement et frottement". In: *Revue Européenne des Éléments Finis* 10.2-4, pp. 489–503. DOI: [10.1080/12506559.2001.11869264](https://doi.org/10.1080/12506559.2001.11869264). eprint: <https://doi.org/10.1080/12506559.2001.11869264>. URL: <https://doi.org/10.1080/12506559.2001.11869264>.
- Moreau, J.J. (1970). "Sur les lois de frottement, de plasticité et de viscosité". In: *Comptes rendus de l'Académie des sciences. Série A - Sciences mathématiques* 271, pp. 608–611.
- (1974). "On Unilateral Constraints, Friction and Plasticity". In: *New Variational Techniques in Mathematical Physics*. Springer Berlin Heidelberg, pp. 171–322. DOI: [10.1007/978-3-642-10960-7\\_7](https://doi.org/10.1007/978-3-642-10960-7_7). URL: [https://link.springer.com/chapter/10.1007/978-3-642-10960-7\\_7](https://link.springer.com/chapter/10.1007/978-3-642-10960-7_7).
- (1986). "Une formulation du contact à frottement sec; application au calcul numérique". In: *Comptes rendus de l'Académie des sciences. Série 2, Mécanique, Physique, Chimie, Sciences de l'univers, Sciences de la Terre* 302.13, pp. 799–801. ISSN: 0764-4450.
- (July 1999). "Numerical aspects of the sweeping process". In: *Computer Methods in Applied Mechanics and Engineering* 177.3-4, pp. 329–349. ISSN: 0045-7825. DOI: [10.1016/S0045-7825\(98\)00387-9](https://doi.org/10.1016/S0045-7825(98)00387-9).
- Murphy, N. and A. Ivankovic (2005). "The prediction of dynamic fracture evolution in PMMA using a cohesive zone model". In: *Engineering Fracture Mechanics* 72.6. Prospects in Fracture Papers from a Conference held to Celebrate the 65th Birthday of Professor J.G. Williams, FRS, FEng Imperial College London, July 2003, pp. 861–875. ISSN: 0013-7944. DOI: <https://doi.org/10.1016/j.engfracmech.2004.08.001>. URL: <http://www.sciencedirect.com/science/article/pii/S001379440400195X>.
- Nguyen, V.P. (2014). "Discontinuous Galerkin/extrinsic cohesive zone modeling: Implementation caveats and applications in computational fracture mechanics". In: *Engineering Fracture Mechanics* 128, pp. 37–68. ISSN: 0013-7944. DOI: <https://doi.org/10.1016/j.engfracmech.2014.07.003>. URL: <http://www.sciencedirect.com/science/article/pii/S0013794414002136>.
- Nguyen, V.P. and J.Y. Wu (Oct. 2018). "Modeling dynamic fracture of solids with a phase-field regularized cohesive zone model". In: *Computer Methods in Applied Mechanics and Engineering* 340, pp. 1000–1022. ISSN: 00457825. DOI: [10.1016/j.cma.2018.06.015](https://doi.org/10.1016/j.cma.2018.06.015).
- Nkoubou Kaptchouang, N.B. et al. (2021). "Cohesive GTN model for ductile fracture simulation". In: *Engineering Fracture Mechanics* 242, p. 107437. ISSN: 0013-7944. DOI: <https://doi.org/10.1016/j.engfracmech.2020.107437>. URL: <https://www.sciencedirect.com/science/article/pii/S0013794420310080>.
- Nocedal, J. and S.J. Wright (1999). *Numerical Optimization*. Springer Verlag.
- Okubo, K. et al. (Nov. 2019). "Dynamics, Radiation, and Overall Energy Budget of Earthquake Rupture With Coseismic Off-Fault Damage". In: *Journal of Geophysical Research: Solid Earth* 124.11, pp. 11771–11801. ISSN: 2169-9313. DOI: [10.1029/2019JB017304](https://doi.org/10.1029/2019JB017304). arXiv: [1901.01771](https://arxiv.org/abs/1901.01771). URL: <https://onlinelibrary.wiley.com/doi/10.1029/2019JB017304>.
- Papoulia, K.D. (2017). "Non-differentiable energy minimization for cohesive fracture". In: *International Journal of Fracture* 204.2, pp. 143–158.
- Papoulia, K.D., C.-H. Sam, and S.A. Vavasis (Oct. 2003). "Time continuity in cohesive finite element modeling". In: *International Journal for Numerical Methods in Engineering* 58.5, pp. 679–701. ISSN: 0029-5981. DOI: [10.1002/nme.778](https://doi.org/10.1002/nme.778). URL: <http://doi.wiley.com/10.1002/nme.778>.
- Parrinello, F. (Sept. 2020). "Hybrid equilibrium element with interelement interface for the analysis of delamination and crack propagation problems". In: *International Journal for Numerical Methods in Engineering* August. ISSN: 0029-5981. DOI: [10.1002/nme.6531](https://doi.org/10.1002/nme.6531). URL: <https://onlinelibrary.wiley.com/doi/10.1002/nme.6531>.
- Parrinello, F. and G. Borino (2020). "Cohesive-frictional interface in an equilibrium based finite element formulation". In: *Proceedings of XXIV AIMETA Conference 2019*. Ed. by Antonio Carcaterra, Achille Paolone, and Giorgio Graziani. Lecture Notes in Mechanical Engineering September. Cham: Springer International Publishing, pp. 419–426. ISBN: 978-3-030-41056-8. DOI: [10.1007/978-3-030-41057-5](https://doi.org/10.1007/978-3-030-41057-5). URL: <http://link.springer.com/10.1007/978-3-030-41057-5>.

- Perales, F. et al. (2010). “A NonSmooth Contact Dynamics-based multi-domain solver”. In: *European Journal of Computational Mechanics* 19.4, pp. 389–417. DOI: [10.3166/ejcm.19.389-417](https://doi.org/10.3166/ejcm.19.389-417). eprint: <https://doi.org/10.3166/ejcm.19.389-417>. URL: <https://doi.org/10.3166/ejcm.19.389-417>.
- Raous, Michel, Laurent Cangémi, and Marius Cocou (1999). “A consistent model coupling adhesion, friction, and unilateral contact”. In: *Computer Methods in Applied Mechanics and Engineering*. DOI: [10.1016/S0045-7825\(98\)00389-2](https://doi.org/10.1016/S0045-7825(98)00389-2). URL: <https://hal.archives-ouvertes.fr/hal-03178187>.
- Remacle, J.-F. et al. (2012). “Blossom-Quad: A Non-Uniform Quadrilateral Mesh Generator Using a Minimum-Cost Perfect-Matching Algorithm”. In: *International Journal for Numerical Methods in Engineering* 89.9, pp. 1102–1119. ISSN: 1097-0207. DOI: [10.1002/nme.3279](https://doi.org/10.1002/nme.3279). URL: <https://onlinelibrary.wiley.com/doi/abs/10.1002/nme.3279> (visited on 07/19/2022).
- Réthoré, J. and R. Estevez (2013). “Identification of a cohesive zone model from digital images at the micron-scale”. In: *Journal of the Mechanics and Physics of Solids* 61.6, pp. 1407–1420. ISSN: 00225096. DOI: [10.1016/j.jmps.2013.01.011](https://doi.org/10.1016/j.jmps.2013.01.011).
- Sam, C.-H., K.D. Papoulia, and S.A. Vavasis (Sept. 2005). “Obtaining initially rigid cohesive finite element models that are temporally convergent”. In: *Engineering Fracture Mechanics* 72.14, pp. 2247–2267. ISSN: 00137944. DOI: [10.1016/j.engfracmech.2004.12.008](https://doi.org/10.1016/j.engfracmech.2004.12.008). URL: <https://linkinghub.elsevier.com/retrieve/pii/S0013794405000895>.
- Samimi, M., J.A.W. van Dommelen, and M.G.D. Geers (Dec. 2011). “A three-dimensional self-adaptive cohesive zone model for interfacial delamination”. In: *Computer Methods in Applied Mechanics and Engineering* 200.49-52, pp. 3540–3553. ISSN: 0045-7825. DOI: [10.1016/J.CMA.2011.08.021](https://doi.org/10.1016/J.CMA.2011.08.021).
- Savitzky, A. and M.J.E. Golay (1964). “Smoothing and Differentiation of Data by Simplified Least Squares Procedures”. In: *Analytical Chemistry* 36.8, pp. 1627–1639. ISSN: 15206882. DOI: [10.1021/ac60214a047](https://doi.org/10.1021/ac60214a047).
- Schlömer, N. (2022). *meshio: Tools for mesh files*. DOI: [10.5281/zenodo.1173115](https://doi.org/10.5281/zenodo.1173115). URL: <https://github.com/nschloe/meshio>.
- Seagraves, A. and R. Radovitzky (2010). *Advances in cohesive zone modeling of dynamic fracture*, pp. 349–405. DOI: [10.1007/978-1-4419-0446-1\\_12](https://doi.org/10.1007/978-1-4419-0446-1_12).
- Talon, C. and A. Curnier (2003). “A model of adhesion coupled to contact and friction”. In: *European Journal of Mechanics - A/Solids* 22.4, pp. 545–565. ISSN: 0997-7538. DOI: [https://doi.org/10.1016/S0997-7538\(03\)00046-9](https://doi.org/10.1016/S0997-7538(03)00046-9). URL: <https://www.sciencedirect.com/science/article/pii/S0997753803000469>.
- Vargas, R. et al. (Dec. 2020). “On the identification of cohesive zone model for curved crack in mortar”. In: *Strain* 56.6. ISSN: 0039-2103. DOI: [10.1111/str.12364](https://doi.org/10.1111/str.12364). URL: <https://doi.org/10.1111/str.12364%20https://onlinelibrary.wiley.com/doi/10.1111/str.12364>.
- Vavasis, S.A., K.D. Papoulia, and M.R. Hirmand (2020). “Second-order cone interior-point method for quasistatic and moderate dynamic cohesive fracture”. In: *Computer Methods in Applied Mechanics and Engineering* 358, p. 112633. ISSN: 0045-7825. DOI: <https://doi.org/10.1016/j.cma.2019.112633>. URL: <https://www.sciencedirect.com/science/article/pii/S0045782519305171>.
- Versino, D. et al. (2015). “A thermodynamically consistent discontinuous Galerkin formulation for interface separation”. In: *Composite Structures* 133, pp. 595–606. ISSN: 0263-8223. DOI: <https://doi.org/10.1016/j.compstruct.2015.07.080>. URL: <http://www.sciencedirect.com/science/article/pii/S0263822315006261>.
- Wright, S.J. (1996). *Primal-Dual Interior-Point Methods*. Philadelphia: SIAM.
- Xu, X.-P. and A. Needleman (Sept. 1994). “Numerical simulations of fast crack growth in brittle solids”. In: *Journal of the Mechanics and Physics of Solids* 42.9, pp. 1397–1434. ISSN: 00225096. DOI: [10.1016/0022-5096\(94\)90003-5](https://doi.org/10.1016/0022-5096(94)90003-5). URL: <https://linkinghub.elsevier.com/retrieve/pii/0022509694900035>.
- Zhang, Z., G.H. Paulino, and W. Celes (Nov. 2007). “Extrinsic cohesive modelling of dynamic fracture and microbranching instability in brittle materials”. In: *International Journal for Numerical Methods in Engineering* 72.8, pp. 893–923. ISSN: 00295981. DOI: [10.1002/nme.2030](https://doi.org/10.1002/nme.2030). URL: <http://doi.wiley.com/10.1002/nme.2030>.
- Zhou, F. and J.-F. Molinari (Jan. 2004a). “Dynamic crack propagation with cohesive elements: a methodology to address mesh dependency”. In: *International Journal for Numerical Methods in Engineering* 59.1, pp. 1–24. ISSN: 0029-5981. DOI: [10.1002/nme.857](https://doi.org/10.1002/nme.857). URL: <http://doi.wiley.com/10.1002/nme.857>.
- (Nov. 2004b). “Stochastic fracture of ceramics under dynamic tensile loading”. In: *International Journal of Solids and Structures* 41.22-23, pp. 6573–6596. ISSN: 00207683. DOI: [10.1016/j.ijsolstr.2004.05.029](https://doi.org/10.1016/j.ijsolstr.2004.05.029).